Cell Reports

Article

Molecular cascade reveals sequential milestones underlying hippocampal neural stem cell development into an adult state

Graphical abstract

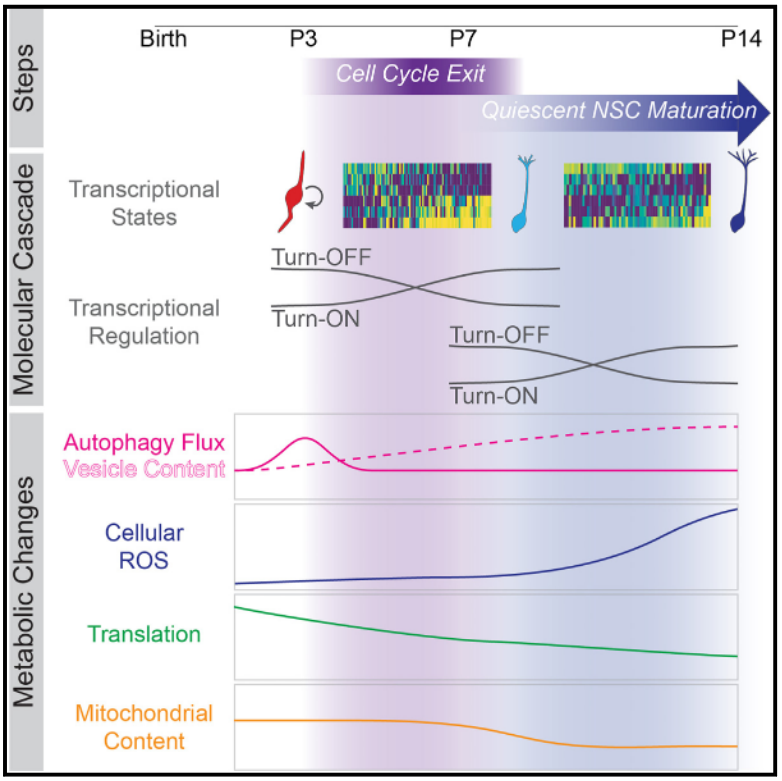

Highlights

- NSC development into an adult state is a multi-step process with defined milestones
- Molecular cascade underlying NSC quiescence acquisition and subsequent maturation
- Sequential metabolic changes in autophagy and ROS during NSC development
- Autophagy promotes NSC quiescence during early postnatal development

Authors

Dennisse Jimenez-Cyrus, Vijay S. Adusumilli, Max H. Stempel, Sandra Maday, Guo-li Ming, Hongjun Song, Allison M. Bond

Correspondence

shongjun@pennmedicine.upenn.edu (H.S.), allison.bond@mssm.edu (A.M.B.)

In brief

Jimenez-Cyrus et al. report the molecular cascade underlying the neural stem cell transition to the quiescent adult state in the early postnatal mouse dentate gyrus. Neural stem cells sequentially progress through multiple states accompanied by transcriptional and metabolic changes. Autophagy functionally promotes the neural stem cell transition to quiescence.

Jimenez-Cyrus et al., 2024, Cell Reports *43*, 114339
June 25, 2024 © 2024 The Author(s). Published by Elsevier Inc.
https://doi.org/10.1016/j.celrep.2024.114339

CellPress

Cell Reports

CellPress
OPEN ACCESS

Article

Molecular cascade reveals sequential milestones underlying hippocampal neural stem cell development into an adult state

Dennisse Jimenez-Cyrus,[1,11] Vijay S. Adusumilli,[1,11] Max H. Stempel,[1] Sandra Maday,[1] Guo-li Ming,[1,2,3,4] Hongjun Song,[1,2,3,5,6,12,*] and Allison M. Bond[1,7,8,9,10,*]

[1]Department of Neuroscience and Mahoney Institute for Neurosciences, Perelman School of Medicine at the University of Pennsylvania, Philadelphia, PA 19104, USA
[2]Department of Cell and Developmental Biology, Perelman School of Medicine at the University of Pennsylvania, Philadelphia, PA 19104, USA
[3]Institute for Regenerative Medicine, University of Pennsylvania, Philadelphia, PA 19104, USA
[4]Department of Psychiatry, Perelman School of Medicine at the University of Pennsylvania, Philadelphia, PA 19104, USA
[5]Department of Neurosurgery, Perelman School of Medicine at the University of Pennsylvania, Philadelphia, PA 19104, USA
[6]The Epigenetics Institute, Perelman School of Medicine at the University of Pennsylvania, Philadelphia, PA 19104, USA
[7]Nash Family Department of Neuroscience, Icahn School of Medicine at Mount Sinai, New York, NY 10029, USA
[8]Department of Cell, Developmental and Regenerative Biology, Icahn School of Medicine at Mount Sinai, New York, NY 10029, USA
[9]Friedman Brain Institute, Icahn School of Medicine at Mount Sinai, New York, NY 10029, USA
[10]Black Family Stem Cell Institute, Icahn School of Medicine at Mount Sinai, New York, NY 10029, USA
[11]These authors contributed equally
[12]Lead contact
*Correspondence: shongjun@pennmedicine.upenn.edu (H.S.), allison.bond@mssm.edu (A.M.B.)
https://doi.org/10.1016/j.celrep.2024.114339

SUMMARY

Quiescent adult neural stem cells (NSCs) in the mammalian brain arise from proliferating NSCs during development. Beyond acquisition of quiescence, an adult NSC hallmark, little is known about the process, milestones, and mechanisms underlying the transition of developmental NSCs to an adult NSC state. Here, we performed targeted single-cell RNA-seq analysis to reveal the molecular cascade underlying NSC development in the early postnatal mouse dentate gyrus. We identified two sequential steps, first a transition to quiescence followed by further maturation, each of which involved distinct changes in metabolic gene expression. Direct metabolic analysis uncovered distinct milestones, including an autophagy burst before NSC quiescence acquisition and cellular reactive oxygen species level elevation along NSC maturation. Functionally, autophagy is important for the NSC transition to quiescence during early postnatal development. Together, our study reveals a multi-step process with defined milestones underlying establishment of the adult NSC pool in the mammalian brain.

INTRODUCTION

Neural stem cells (NSCs) supply the mammalian brain with new neurons and glia.[1] NSCs persist in adulthood in a quiescent state in two niches, the subventricular zone (SVZ) of the lateral ventricles and the subgranular zone (SGZ) in the dentate gyrus (DG) of the hippocampus.[2,3] Quiescent NSCs in the adult SGZ can reactivate to generate DG granule neurons that integrate into the existing hippocampal circuitry, contributing to learning and memory and affective cognition.[4–7] Conversely, dysregulated adult hippocampal neurogenesis is associated with neurological disorders, such as depression, epilepsy, and Alzheimer's disease.[7–10] The capacity for adult neurogenesis-associated plasticity is ultimately dependent on the source of new neurons, the quiescent adult NSC pool. However, the adult NSC pool is finite and depletes as adulthood progresses, resulting in an age-dependent decline in neurogenesis and cognitive function.[11–14] Therefore, the capacity for lifelong neurogenesis-associated plasticity is determined by the initial establishment of the quiescent adult NSC pool during early postnatal development.[15,16] Very little is known about how the adult NSC pool is established,[17,18] information that will be key to understanding how NSCs persist beyond development to contribute to adult neuroplasticity.

Quiescence, a non-dividing state from which cells can reenter cell cycle, is a defining feature of adult stem cells in many somatic tissues,[19,20] and the transition to quiescence is the only known major milestone that marks the shift from a developmental to an adult NSC state in both the SGZ and SVZ.[15,16,21,22] Adult SGZ NSCs originate from a *Hopx*-expressing lineage of NSCs that shift to quiescence during early postnatal development.[16] Other properties, such as morphology and localization,[16,23–25] cell division and self-renewal properties,[26–29] and molecular signatures,[16,30,31] also distinguish

This is an open access article under the CC BY-NC-ND license (http://creativecommons.org/licenses/by-nc-nd/4.0/).

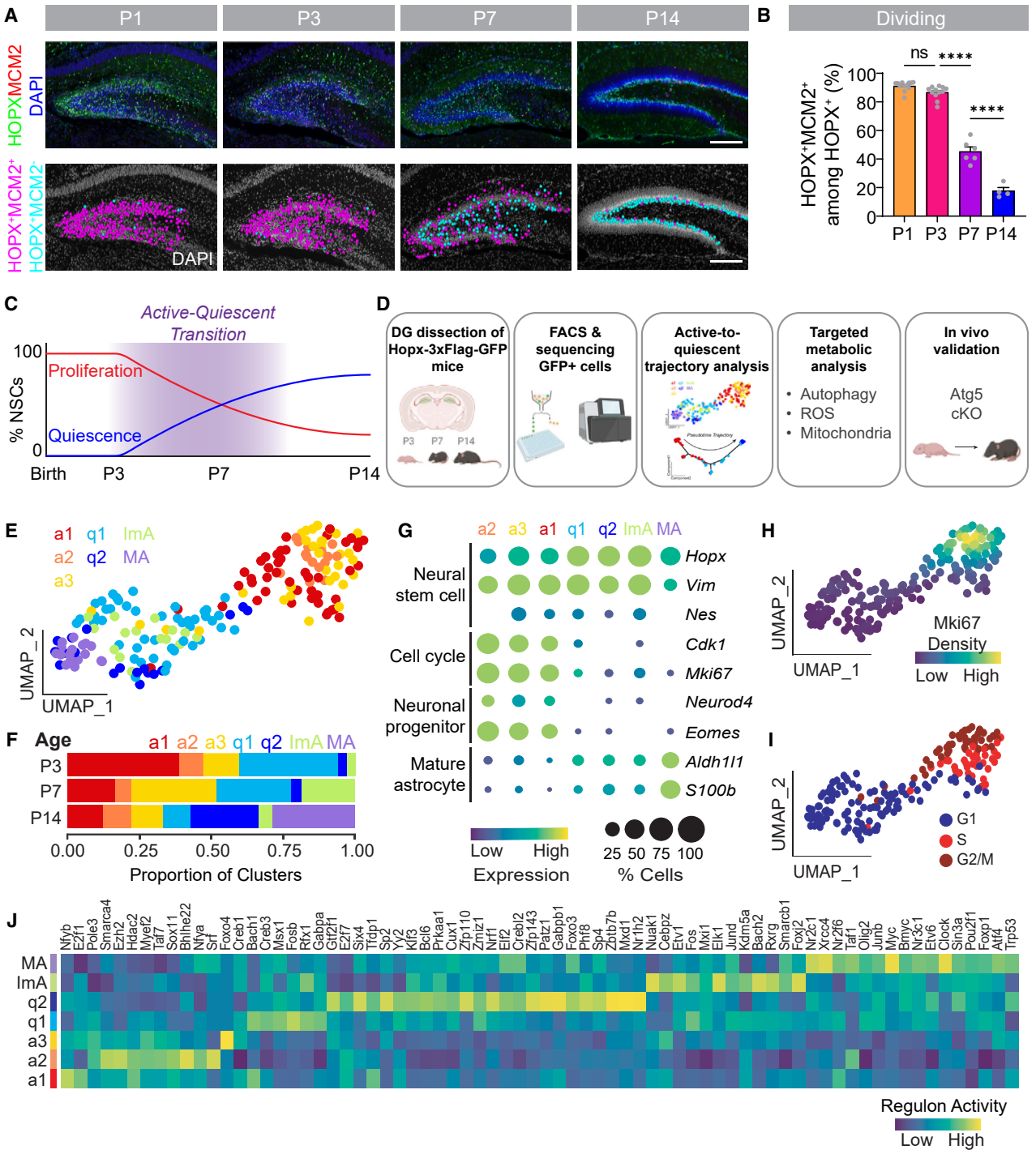

Figure 1. Single-cell RNA-sequencing reveals transcriptomic states of NSCs during the transition to a quiescent adult state

(A) Sample confocal images of HOPX$^+$MCM2$^+$ dentate gyrus (DG) NSCs at P1, P3, P7, and P14 from *Hopx-3xFlag-GFP* mice (top panels) and corresponding diagrams of dividing HOPX$^+$MCM2$^+$ NSCs (pink dots) and non-dividing HOPX$^+$ MCM2$^-$ NSCs (blue dots). Scale bars, 200 μm.

(B) Quantification of the percentage of MCM2$^+$ cells among all HOPX$^+$ NSCs in the DG. Each dot represents data from one mouse. Values represent mean ± SEM (n = 4–12 mice; ****$p < 0.0001$; ns: $p > 0.05$; one-way ANOVA with Tukey's post hoc test).

(C) Timeline of the DG NSC transition from an active to quiescent state across early postnatal development (postnatal day 3 [P3], P7, and P14).

(D) GFP$^+$ cells were isolated from the DG of *Hopx-3xFlag-GFP* mice at P3, P7, and P14 for single-cell RNA-sequencing (scRNA-seq; Figures 1, 2, 3, and 4), which informed a targeted metabolic analysis (Figure 5) and an *in vivo* functional assay to validate autophagy as a regulator of NSC development (Figure 6).

(legend continued on next page)

developmental NSCs from adult NSCs, but the timing of these changes and their contribution to the adult NSC state remain unknown. A detailed analysis during critical developmental stages is required to fill these gaps and reveal mechanisms that drive NSC development into an adult state and establishment of the adult NSC pool. Given that somatic stem cells in many tissues undergo a developmental shift from a proliferating to a quiescent state, knowledge gained from DG NSC development may provide insight into the establishment of adult somatic stem cells in other tissues.[19]

Distinct metabolic states are associated with stem cell function.[32] For example, adult NSCs are generally characterized by low levels of transcription, translation, and ribosome biogenesis and favor glycolysis to oxidative phosphorylation as their primary energy source.[19,20,33] In contrast, as adult NSCs differentiate, they exhibit higher levels of transcription, translation, and ribosome biogenesis and favor oxidative phosphorylation.[34] Recent studies suggest that certain aspects of cellular metabolism, like the lysosomal pathway and lipogenesis, regulate NSC activation from quiescence.[35,36] In addition, fatty acid oxidation and mitochondrial pyruvate metabolism are required to maintain quiescence.[37,38] Despite what we have begun to learn about the metabolic control of adult NSCs, little is known about how cellular metabolism may regulate NSC development and the transition into a quiescent adult state.

Here we took advantage of the genetic marking of *Hopx*-expressing DG NSCs in mice[16] and applied single-cell RNA-sequencing to construct a molecular cascade of gene expression changes underlying NSC development into an adult state. We found that NSC development into an adult state is a protracted, multi-step process, rather than an abrupt switch that occurs as NSCs enter quiescence. We further identified a sequence of molecular, cellular, and metabolic milestones that mark each developmental step and showed that autophagy promotes the NSC transition to quiescence during early postnatal development. Collectively, our results delineate a previously unstudied developmental process that is critical to establishing the adult NSC pool in the mammalian hippocampus and support the notion that NSCs in the DG undergo continuous development across the lifespan.

RESULTS

NSCs exist in multiple proliferative and quiescent states during early postnatal development

We investigated changes in DG NSC properties at multiple time points across early postnatal development (postnatal day 1 [P1], P3, P7, P14) that encompass the transition to quiescence using the *Hopx-3xFlag-GFP* mouse line,[39] which labels DG NSCs, including a lineage that acquires quiescence to establish the adult SGZ NSC pool.[16] First, we performed immunostaining of MCM2, a cell cycle marker expressed during all cell cycle phases (G1–S–G2–M) but rapidly downregulated during cell cycle exit (G0),[40,41] to determine when DG NSCs exit the cell cycle during the early postnatal period. We found that the majority of the HOPX$^+$ NSC population in the DG was MCM2$^+$ at P1 and P3, and it was not until P7 that a significant proportion of NSCs was MCM2$^-$ and had exited the cell cycle (Figures 1A–1C), confirming our previous finding.[16] The majority of NSCs were quiescent and located in the SGZ by P14 (Figure 1A), a stage when the adult neurogenic niche is clearly delineated.[25] We wondered if changes in cell cycle phase occupancy between P1 and P3 might precede the NSC shift to quiescence. Using GEMININ to mark the S/G2/M phases of cell cycle,[42] we found that the proportion of HOPX$^+$MCM2$^+$ NSCs in the S/G2/M phase increased from P1 to P3, and this increase was sustained at P7 (Figures S1A and S1B). Then, we used histone H3 phosphorylated on serine 10 (PH3) to identify dividing NSCs that were in the G2/M phases of cell cycle. We found that the proportion of HOPX$^+$MCM2$^+$ NSCs in the G2/M phases also increased from P1 to P3, and this increase was sustained at P7 (Figures S1C and S1D). These results showed that DG NSCs increased their occupancy in the S/G2/M phases before exiting cell cycle, suggesting that some changes in NSC properties may not be coupled to the shift to quiescence.

Next, we used single-cell RNA-sequencing (scRNA-seq) as a global approach to identify a transcriptome-wide molecular cascade in DG NSCs as they transition into a quiescent state during early postnatal development. We dissected DGs from *Hopx-3xFlag-GFP* mice at P3, P7, and P14, time points that span the transition into quiescence[16] (Figure 1C) and isolated HOPX-GFP$^+$ cells via fluorescence-activated cell sorting (FACS) for scRNA-seq analysis using SMART-seq2 to have better coverage of transcripts[43] (Figure 1D; Table S1). After quality control and removal of a small number of ependymal cells, our dataset formed six clusters via unsupervised clustering (Figures S1E and S1F; Table S1). Because *Hopx* is also expressed in a limited number of DG astrocytes,[44] we used *Abhd3*, *Gjb6*, and *Gabrg1* co-expression[31,45] as the criteria to delineate a seventh cluster containing mature astrocytes (Figures 1E, S1G, and S1H). The mature astrocyte cluster (MA) only included cells from P14 (Figure 1F), had high expression of astrocyte marker genes (Figures 1G and S1I), and its transcriptome correlated with mature astrocytes from a previous hippocampal scRNA-seq dataset[31] (Figure S1J). Among the

(E) UMAP of all cells (excluding ependymal cells) analyzed by scRNA-seq in (D) separated into 7 clusters (a1, active-1; a2, active-2; a3, active-3; q1, quiescent-1; q2, quiescent-2; ImA, immature astrocyte; MA, mature astrocyte) based on unsupervised Monocle2 clustering and supervised identification of a mature astrocyte cluster.
(F) Bar graph of the distribution of cells in each cluster at different ages.
(G) Bubble plot of sample cell-type-specific marker gene expression in each cluster.
(H) Kernel density estimation plot showing the distribution of Mki67 in each cell on the UMAP (E).
(I) Predicted cell cycle phase (G1, S, and G2/M) in each cell on the UMAP (E).
(J) Heatmap of regulon activity in each cluster calculated by gene regulatory network (GRN) analysis.
See also Figure S1.

seven clusters, we also identified an immature astrocyte cluster (ImA), which was largely composed of cells from P7 (Figure 1F), had moderate expression of astrocyte marker genes (Figure S1I), and its transcriptome also correlated with immature astrocytes from a previous hippocampal scRNA-seq dataset[31] (Figure S1J). The remaining five clusters represented different NSC states based on marker expression: three clusters (a1, a2, and a3) represented actively dividing NSC states, and two clusters (q1 and q2) represented quiescent NSC states (Figure 1G). Cells from actively dividing states (Mki67^{high}) grouped together in one corner of the Uniform Manifold Approximation and Projection (UMAP), and cells from quiescent states (Mki67^{low}) grouped together in the opposing corner (Figure 1H). Each dividing cluster and age included cells from multiple phases of the cell cycle (Figures S1K and S1L), and cells in each cell cycle phase grouped together on the UMAP (Figure 1I). Each NSC state had a unique age distribution (Figures 1F and S1M) and distinct gene regulatory network (GRN) activity (Figure 1J). Together, this analysis provided a transcriptional atlas of multiple NSC states that exist during the transition to quiescence.

NSCs continue to mature after quiescence acquisition

Next, we used RNA velocity,[46] a high-dimensional vector that represents the predicted future state of individual cells,[46] to determine which cluster(s) of actively dividing NSCs were most likely transitioning into quiescence. We found that large RNA velocities in the a1 group pointed toward the q1 cluster, whereas only small, randomly directed velocities were found in the a2 and a3 dividing NSC clusters, suggesting that a2 and a3 were either in a steady state or their future state was not present in the cells analyzed (Figure 2A). Removing the astroglial clusters (ImA and MA) resulted in similar RNA velocities in the a1 group pointed toward the q1 cluster (Figure S2A). In addition, we found that the a2 and a3 groups had higher cell cycle scores than the a1 group, indicating lower cell cycle gene expression in a1 (Figure 2B). Together, these data suggested that the a1 dividing NSC cluster was most likely transitioning into a quiescent state.

We then focused our analysis on a1, q1, and q2. Large RNA velocities in the q1 cluster pointed toward the q2 cluster, suggesting that cells dynamically moved through q1 into q2 (Figure 2A). We generated an inferred pseudotime trajectory that ordered the cells into sequential transcriptional states beginning with a1, followed by q1 and then q2 (Figures 2C, 2D, and S2B). Following the real-time developmental time course, the first half of the pseudotime was dominated by cells from P3 and P7, while the second half of the pseudotime contained many cells from P14 (Figures 2D and S2C). We found that only cells in a1 had a positive cell cycle score, indicating that they were dividing, while cells in q1 and q2 expressed very low levels of cell cycle genes (Figures 2E and 2F). In contrast, we found that an Adult NSC score associated with quiescent adult NSC gene expression[34] gradually increased along the pseudotime (Figure 2D). The Adult NSC score increased from a1 to q1 and from q1 to q2, suggesting that adult NSC gene expression continues to increase after cell cycle exit (Figures 2G and 2H). The quiescent clusters followed developmental age, with q1 dominant at P3/P7 and q2 dominant at P14 (Figure 2I). We also observed progressive acquisition of the adult NSC signature with age (Figure S2D). We wondered if the adult NSC signature strengthens beyond P14, so we integrated our early postnatal dataset with our previously published adult NSC dataset,[34] which included 5 clusters that spanned the beginning of the neurogenic lineage from quiescent NSC (S1, S2, and S3) to active NSC/early neuronal progenitor (S4 and S5). We observed overlap between datasets but segregation of dividing clusters and quiescent clusters (Figures S2E and S2F). Our q1 and q2 quiescent clusters were most similar to the S2 cluster in the adult NSC dataset but less similar to the S1 cluster, which anchors the quiescent end of the pseudotime[34] (Figure S2G), suggesting that quiescent NSCs continue to mature beyond P14.

Together, these data suggest that acquisition of an adult NSC state is a multi-step developmental process: NSCs first exit the cell cycle and enter an immature quiescent state between P3 and P7, and then they undergo further maturation between P7 and P14 toward an adult NSC state (Figure 2J).

Distinct molecular landscapes characterize each step of NSC development

We conducted GRN analysis on each step of the pseudotime (a1 to q1 and q1 to q2) to identify distinct gene networks that characterize each step of NSC development. The GRN score considers changes in expression of the transcriptional regulator and its predicted target genes, collectively called a regulon. We found that transcriptional regulator expression cascaded across the pseudotime (Figure 3A), and we identified regulons that were either increased or decreased across the a1 to q1 step (Figures 3B and 3C) and the q1 to q2 step (Figures 3D and 3E). Interestingly, some regulons only changed across one step, like *Nfix* and *Hlf*, while others continuously changed across the entire pseudotime, like *Rps3* and *Sox9*. Immunostaining confirmed that NFIX protein expression was lower in quiescent NSCs (HOPX^{+}MCM2^{-}) than proliferating NSCs (HOPX^{+}MCM2^{+}) at P7 and P14 (Figures 3F and 3G), and that SOX9 protein expression was higher in quiescent NSCs than proliferating NSCs at P7 and P14 (Figures 3H and 3I). Notably, regulons that changed across both steps often had a different composition of target genes across each step, and a target gene's contribution to the regulon could be different across each step (Figures S3A and S3B). Some of the identified regulons, like *Sox11* and *Nfix*, are known to be required for proper DG morphogenesis during development.[47–49] Others, like *Npas3*, a transcription factor implicated in schizophrenia and intellectual disability,[50–52] are known to be required for normal proliferation and neurogenesis in the adult mouse DG.[53] We also identified regulons that have no known role in regulating NSCs, like *Hlf*, which maintains hematopoietic stem cell quiescence.[54–56] Collectively, these results revealed distinct gene networks underlying each step of NSC development into an adult state.

Metabolism-related gene expression changes with each step of NSC development

Next, we elucidated the impact of gene expression changes on cell biology in each step of NSC development. We identified kinetic patterns of gene expression across the a1 to q1 and q1 to q2 steps of the pseudotime using CellRouter[57] (Figures 4A

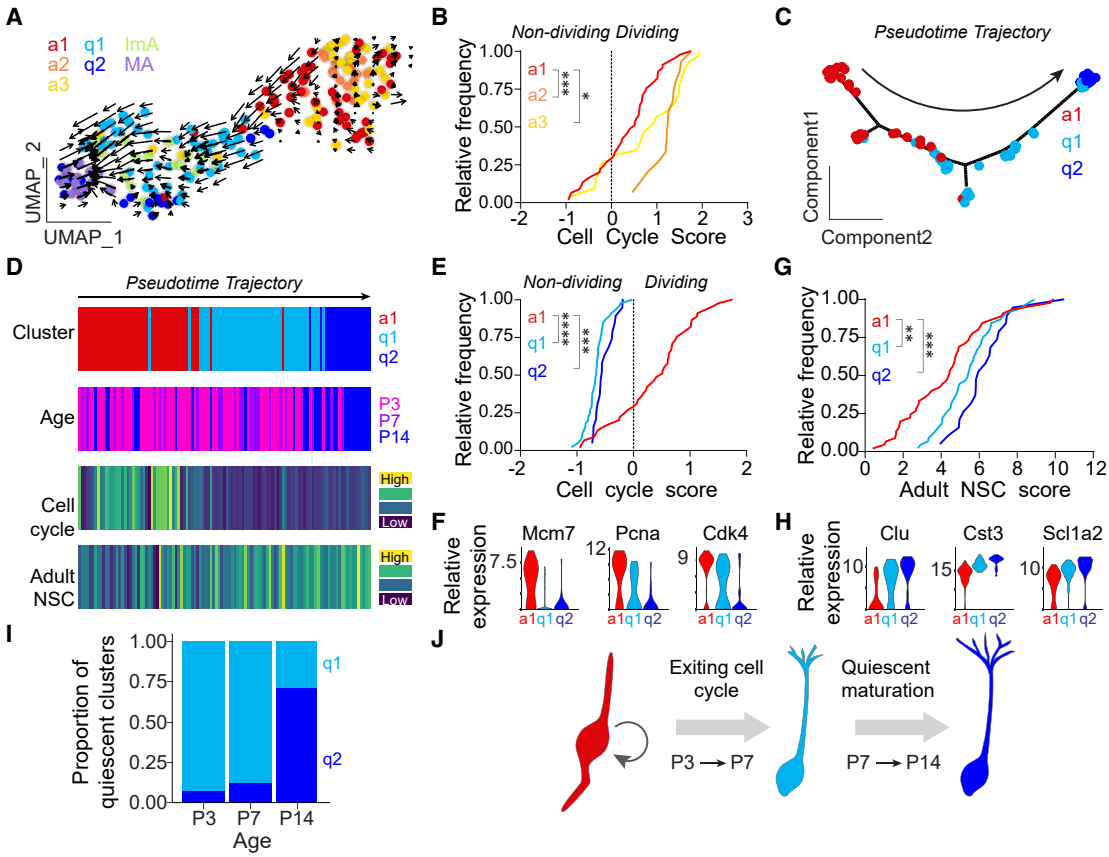

Figure 2. NSCs exit cell cycle and undergo additional maturation before reaching an adult state

(A) RNA velocity vectors overlaid on the cluster UMAP (Figure 1E).

(B) Distribution curve of cell cycle scores for individual cells of all three active clusters (a1, a2, and a3; *$p < 0.05$, ***$p < 0.001$; Kruskal-Wallis rank-sum test with Dunn's post hoc test).

(C) Principal component analysis (PCA) showing the pseudotime trajectory of cells from clusters a1, q1, and q2 that represents the NSC transition to a quiescent adult state. Arrow indicates direction of pseudotime trajectory.

(D) Heatmaps of cell cycle scores and adult NSC scores of individual cells in pseudotime order with the corresponding cluster and age identification. Cell cycle score was calculated as in (B).

(E) Distribution curve of cell cycle scores for individual cells from clusters a1, q1, and q2 (***$p < 0.001$, ****$p < 0.0001$; Kruskal-Wallis rank-sum test with Dunn's post hoc test).

(F) Violin plots of sample cell cycle gene expression for clusters a1, q1, and q2.

(G) Distribution curve of adult NSC scores for individual cells from clusters a1, q1, and q2 (**$p < 0.01$, ***$p < 0.001$; Kruskal-Wallis rank-sum test with Dunn's post hoc test).

(H) Violin plots of sample adult NSC gene expression for clusters a1, q1, and q2.

(I) Bar plot of the proportion of cells in quiescent NSC clusters (q1 and q2) at each age.

(J) Graphical summary showing that DG NSCs first exit cell cycle between P3 to P7 and then acquire a more mature transcriptomic signature from P7 to P14.

Also see Figure S2 and Table S1.

and 4B; Table S2) and performed Gene Ontology (GO) analysis on each kinetic pattern (Figures 4A and 4B; Table S3). Genes related to transcription and RNA splicing decreased in expression across the a1 to q1 step of quiescence acquisition (Figures 4A and S4A). Interestingly, we found increased expression of genes involved in cell junction assembly, protein catabolism, and autophagy along the a1 to q1 trajectory (Figures 4A and S4A). Genes involved in autophagy were specifically upregulated in the q1 state (Figure 4C). Genes involved in the establishment of cell polarity and metabolic processes, such as ATP metabolic process and energy derivation by oxidation of organic compounds, increased in expression across the q1 to q2 step of NSC maturation (Figures 4B and S4B). Some biological processes, like those related to mitochondrion organization and translation, exhibited gene expression changes across both steps of the trajectory (Figures 4A, 4B, S4A, and S4B). Decreased expression of genes related to translation indicated downregulation of protein synthesis at the cell cycle exit step and the maturation step (Figure 4D), which we confirmed in an independent assay that measured global protein translation using OPP (O-propargyl-puromycin) incorporation (Figures 4E–4G). Together, these results revealed a timeline of cell biology

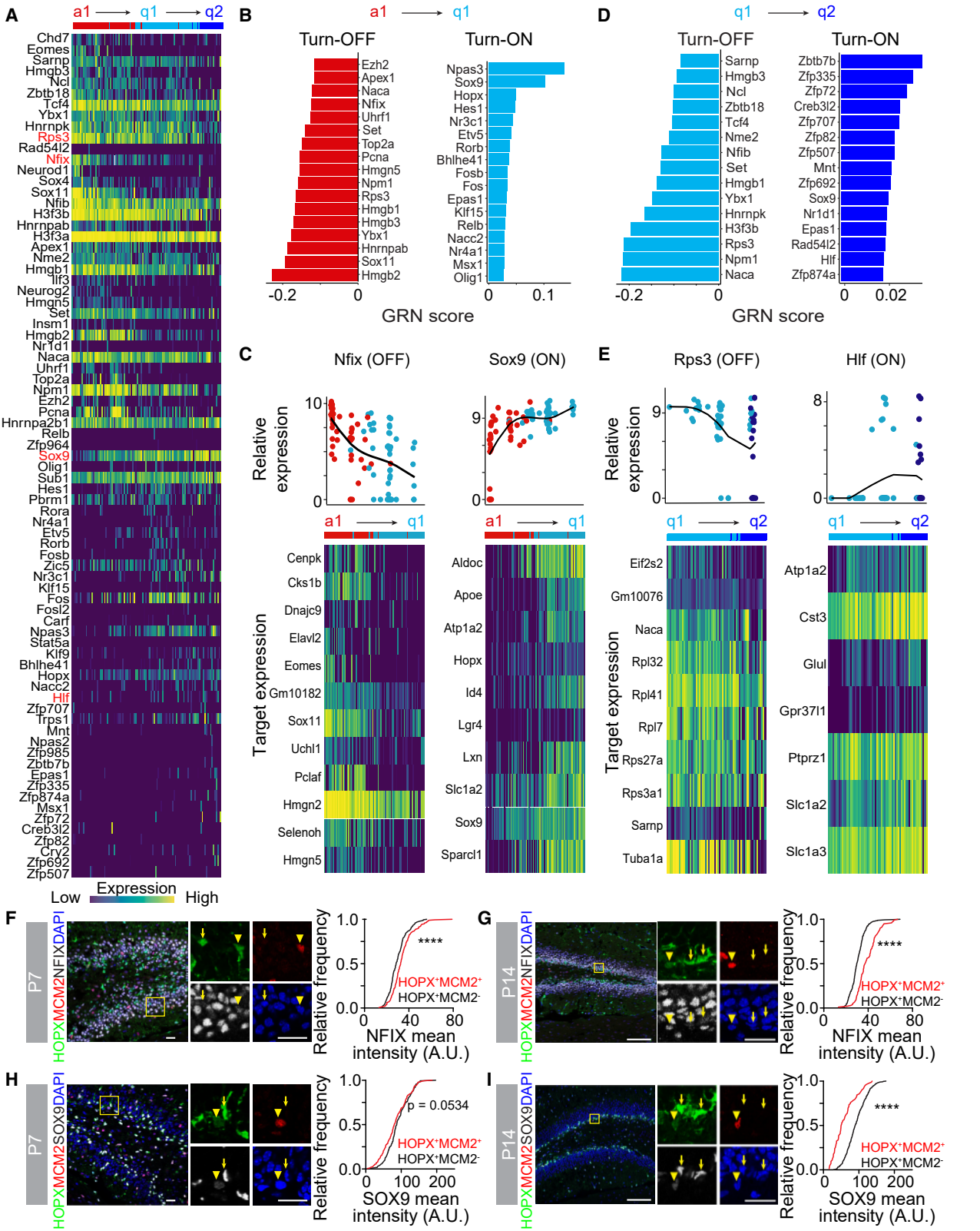

(legend on next page)

changes during NSC development into an adult state and highlighted a significant metabolic transformation.

Sequential metabolic milestones mark each step of NSC development

To test whether distinct metabolic changes indeed underlie each step of NSC development at the cellular level, we used cell permeable dyes and flow cytometry to experimentally assess multiple metabolic parameters in individual DG NSCs isolated from *Hopx-3xFlag-GFP* mice at P3, P7, and P14 (Figures 5A and S5A).

Autophagy is a conserved catabolic process that degrades and recycles intracellular components for turnover of cytoplasmic content, but autophagy can also be induced in response to stress to eliminate toxic or damaged components and to serve as a source of energy.[58,59] Previous studies suggested that autophagy may be important for DG development,[60] as well as for proliferation and survival of adult NSCs and their progeny.[61,62] Given our observation that autophagy-related genes were upregulated as NSCs exited the cell cycle (Figures 4A and 4C), we examined whether changes in autophagy might occur in sync with cell cycle exit between P3 and P7. We used the commercial Autophagy Assay Kit (Red),[63] which labels autophagosomes and autolysosomes (Figure S5B), and we confirmed the specificity of the dye using cells derived from transgenic mice expressing GFP-LC3[64–66] (Figure S5C). We found that autophagic vesicle content increased in NSCs (GFP^+) from P3 to P7, and this higher level was maintained at P14 and 6 weeks (Figures 5B–5D and S5E). An increase in autophagic vesicle content can correspond to enhanced autophagy, but it can also occur if lysosomal degradation is reduced.[67] We measured autophagic flux in NSCs using treatment with chloroquine to distinguish between these two possibilities.[68] We found that the NSC autophagic flux was highest at P3 and decreased to low basal levels at P7 and P14 (Figures 5F and 5G). Increased autophagic flux at P3 was confirmed using bafilomycin A1[67,68] (Figure 5H). To examine whether high autophagic flux might simply be correlated with NSC proliferation, we also measured autophagic flux at P1, another age when the majority of NSCs are dividing (Figures 1A and 1B). To our surprise, we found that NSCs had a low basal level of autophagic flux at P1, similar to P7 and P14 (Figures 5F and 5G). Together, these results demonstrated that NSCs undergo a burst of autophagic flux at P3, right as they prepare to exit cell cycle. Importantly, NSCs exhibited a distinct developmental trajectory of autophagic vesicle content and flux compared to the surrounding cellular environment (GFP^-), suggesting that temporal changes in autophagy are specific to NSC development, rather than a tissue-wide phenomenon (Figures 5E, S5D, and S5F).

Redox balance and buildup of cellular reactive oxygen species (ROS) contributes to oxidative stress that can be toxic for the cell, but ROS can also function as a second messenger signal.[69–71] High levels of cellular ROS are associated with the adult quiescent NSC state in the DG,[72] but cellular ROS levels in developmental NSCs have not been studied. We used the superoxide indicator dihydroethidium (DHE)[72] to measure cellular ROS levels in NSCs across early postnatal development (Figure 5A). We found that cellular ROS was relatively low in NSCs (GFP^+) at P3 and P7, similar to the surrounding cellular environment (GFP^- cells; Figures 5I–5L). However, levels of cellular ROS markedly increased in NSCs at P14 and furthermore at 6 weeks, distinguishing them from the surrounding cellular environment in the DG (Figures 5I–5L, S5G, and S5H). These results demonstrated that the high ROS level associated with the adult quiescent NSC state in the DG is acquired after P7 and is associated with NSC maturation after quiescence.

Mitochondrial function is critical for NSC self-renewal, proliferation, and differentiation,[73] but mitochondrial respiration is also a major source of cellular ROS.[74] We wondered if the increased cellular ROS associated with the quiescent NSC state was due to changes in mitochondria. We used MitoTracker Deep Red staining[75] to show that mitochondrial mass did not significantly differ in DG NSCs between P3 and P7, but it was reduced after P7 at P14 and 6 weeks (Figures S5I–S5K). The changes in mitochondrial mass were anti-correlated to the changes in cellular ROS during this period, suggesting that increased cellular ROS in NSCs was not due to increased mitochondrial respiration. The changes in NSC mitochondrial mass and cellular ROS levels both occurred after P7, suggesting that these metabolic transformations were associated with NSC maturation after quiescence acquisition.

Together, these data demonstrate that distinct metabolic milestones occur sequentially during DG NSC development: first, a burst of autophagy flux corresponds to the initiation of the shift to quiescence, and then increased ROS accompanies NSC maturation into an adult state.

Autophagy promotes the NSC transition to quiescence

Timing is key to cellular mechanisms that promote the developmental transition to quiescence. The transient autophagic burst

Figure 3. Distinct gene regulatory network activity at each step of NSC development

(A) Heatmap of transcriptional regulator gene expression across the pseudotime trajectory (Figure 2D) identified by GRN analysis. Transcriptional regulators highlighted in red are plotted in (C) and (E), along with their target gene expression.

(B) Bar plot of regulon GRN scores whose activity turned off (left panel) or turned on (right panel) across the a1 to q1 step of the pseudotime trajectory.

(C) Dot plot of transcriptional regulator gene expression across the a1 to q1 step of the pseudotime (*Nfix* and *Sox9*, upper panels) and heatmap of corresponding target gene expression (lower panels).

(D) Bar plot of regulon GRN scores whose activity turned off (left panel) or turned on (right panel) across the q1 to q2 step of the pseudotime trajectory.

(E) Dot plot of transcriptional regulator gene expression across the q1 to q2 step of the pseudotime (*Rps3* and *Hlf*, upper panels) and heatmap of corresponding target gene expression (lower panels).

(F–I) Sample confocal images of NFIX (F and G) or SOX9 (H and I) expression in $HOPX^+$ NSCs by immunostaining at P7 (F and H) or P14 (G and I) in the DG (left panels). Boxed area is shown at higher magnification (middle panels; arrowheads = dividing [$HOPX^+MCM2^+$] NSCs, arrows = quiescent [$HOPX^+MCM2^-$] NSCs). Scale bars: 20 μm. Cumulative frequency distribution plots of NFIX or SOX9 mean intensity (right panels) in dividing NSCs (red line) and quiescent NSCs (black line). ($n > 300$ cells from 3 mice; $^{****}p < 0.0001$; Kolmogorov-Smirnov test).

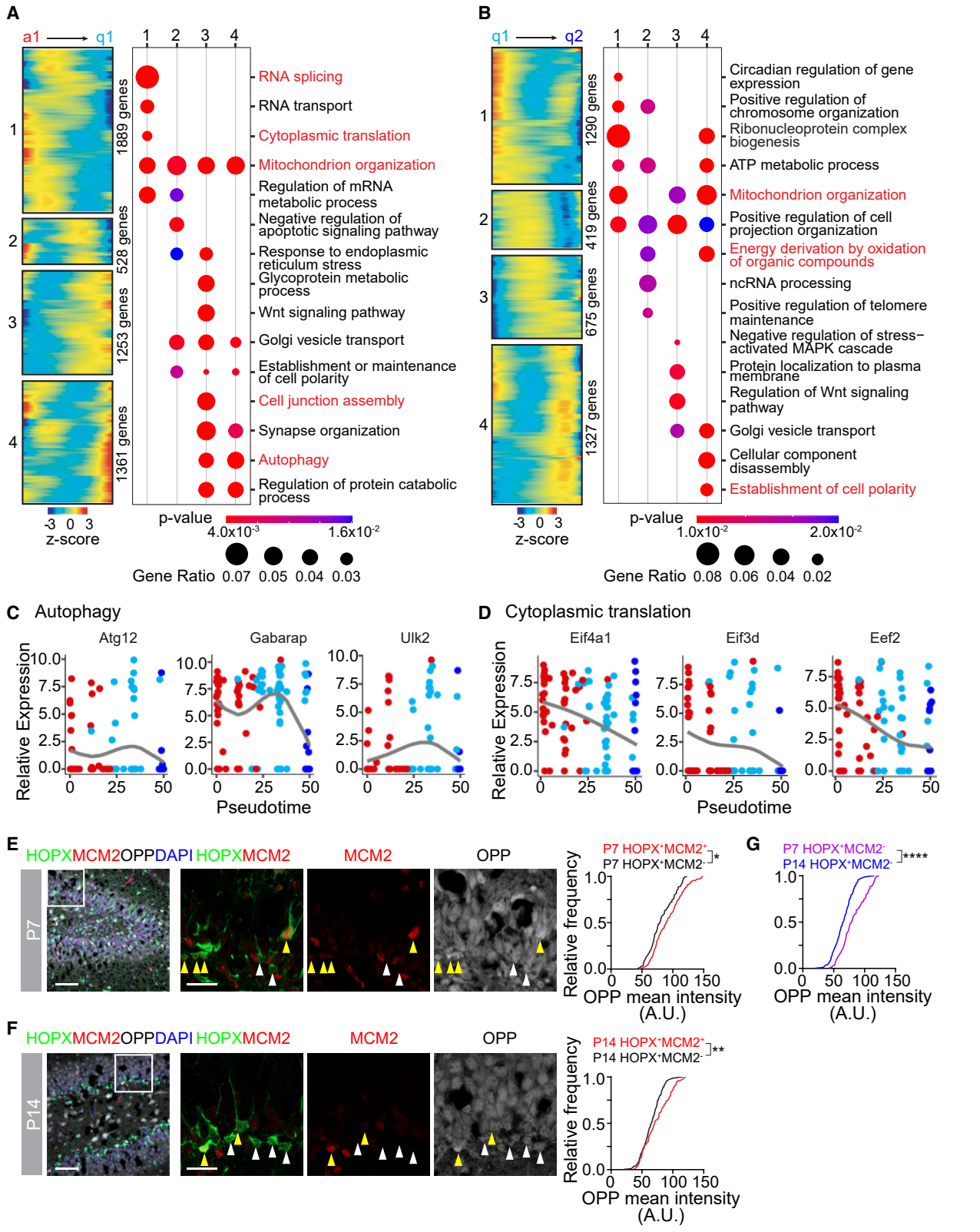

(legend on next page)

at P3, when DG NSCs are on the cusp of transitioning to quiescence, suggested that autophagy may be involved in this developmental transition. To test this hypothesis, we deleted autophagy-related gene 5 (*Atg5*),[76] a critical component of the autophagy machinery that decreased in expression across the pseudotime trajectory (Figure 6A). *Hopx-CreER^{T2}::mTmG Atg5$^{wt/wt}$* and *Hopx-CreER^{T2}::mTmG Atg5$^{Flx/Flx}$* mice were administered tamoxifen at P1, and NSC proliferation was assayed at P7 and P14 (Figure 6B). *Atg5* deletion increased the proportion of DG NSCs that were proliferating (HOPX$^+$MCM2$^+$) but decreased the total number of GFP$^+$ NSCs at both P7 and P14 (Figures 6C–6H). In addition, *Atg5* deletion increased the proportion of GFP$^+$ cells that were neurons (PROX1$^+$) and the total number of GFP$^+$ neurons at both P7 (Figures S6A–S6C) and P14 (Figures S6D–S6F). Together, these results suggest that autophagy promotes quiescence, and in its absence, NSCs continue to divide and generate neurons at the expense of preserving the NSC pool. Thus, autophagy is an important metabolic regulator of DG NSC quiescence acquisition during early postnatal development.

DISCUSSION

Our study reveals the stepwise nature of DG NSC development into an adult state and supports the concept of progressive NSC development. The cellular, molecular, and metabolic changes that collectively underlie development into an adult state occur sequentially, before or after quiescence acquisition, rather than a synchronous switch at cell cycle exit. Using our timeline combined with an *in vivo* functional assay, we identified autophagy as an early mechanism promoting NSC quiescence, consistent with a recent independent study demonstrating a role for Atg7 in the NSC quiescence transition.[18] Insights into the changes identified in this study that underlie NSC development will be critical to revealing the brain's endogenous capacity for neurogenesis-associated plasticity across the lifespan.

Our study attained a high-resolution picture of DG NSC development by analyzing multiple parameters in individual NSCs along a developmentally relevant time course. We analyzed transcriptomic and metabolic changes in a defined population of *Hopx*$^+$ DG NSCs during the critical period of quiescence acquisition and revealed a timeline of defined milestones that underlie NSC development into an adult state. Previous studies have used unbiased scRNA-seq to show that the molecular profile of NSCs changes across embryonic and postnatal development in the neocortex and hippocampus,[31,77] but these studies focused on a single parameter (gene expression) and did not functionally test candidate mechanisms driving development. In contrast, our multimodal approach revealed autophagy as a functional regulator of NSC development into a quiescent state. First, we used our scRNA-seq data to identify two quiescent NSC states that were age segregated to early (P3/7) and late (P14) postnatal development and constructed an inferred developmental trajectory that showed NSCs sequentially progressing from a dividing state to an early quiescent state to a late quiescent state. We identified distinct regulatory landscapes that characterized each step of NSC development, including known transcriptional regulators of DG development[47–49] or adult neurogenesis,[53,78] as well as others that have no known function in DG NSCs, like *Hlf* and *Npm1,* but play a role in hematopoietic stem cell function and leukemia.[54,56,79,80] Next, we demonstrated that distinct metabolic milestones characterize each step of NSC development. A burst of autophagy occurs as NSCs prepare to exit the cell cycle, followed by decreased levels of global translation that occur as NSCs exit cell cycle and continue as quiescent NSCs mature. In addition, after quiescence acquisition, mitochondrial content decreases to a plateau, and levels of cellular ROS significantly increase. Finally, we tested the causal role of autophagy in NSC development and showed that blocking autophagy *in vivo* attenuated the NSC transition into a quiescent adult state.

Our data support a concept of protracted DG NSC development that may extend across the lifespan. The size of the adult DG NSC pool decreases across adulthood,[13,14] and DG NSCs become more dormant with advancing age,[16,81] both of which contribute to reduced levels of neurogenesis in aging.[11,12] More recent studies have identified additional changes in adult NSC properties, such as the capacity for self-renewal, as early as 6 months old in mice, only about 25% of the way through the lifespan.[14,82,83] Together with our findings, these results suggest that the properties of NSCs continue to change well after quiescence acquisition and are likely to undergo a lifelong progression.

Though there is clear evidence that hippocampal neurogenesis occurs throughout adulthood in rodents[27,84–86] and non-human primates,[87–92] there is conflicting evidence for the existence of active neurogenesis in the adult human hippocampus.[93–101] Neurogenesis in adulthood is fundamentally dependent on the

Figure 4. Cell biology changes at each step of NSC development

(A) Heatmaps of gene expression patterns (#1, 2, 3, and 4) across the a1 to q1 step of the pseudotime (left panel) and bubble plots of Gene Ontology (GO) analysis of biological processes analysis of each pattern (right panel). Genes from GO terms in red are plotted in (C) and (D) and Figure S4A.

(B) Heatmaps of gene expression patterns (#1, 2, 3, and 4) across the q1 to q2 step of the pseudotime (left panel) and bubble plots of GO analysis of biological processes analysis of each pattern (right panel). Genes from GO terms in red are plotted in Figure S4B.

(C) Dot plot of autophagy-related gene expression across the pseudotime.

(D) Dot plot of cytoplasmic translation-related gene expression across the pseudotime.

(E and F) Sample confocal images of OPP (O-propargyl-puromycin) staining in dividing (HOPX$^+$MCM2$^+$) and quiescent (HOPX$^+$MCM2$^-$) NSCs at P7 (E) or P14 (F) (left panel). Boxed area is shown at higher magnification (middle panels; yellow arrowheads = dividing [HOPX$^+$MCM2$^+$] NSCs, white arrowheads = quiescent [HOPX$^+$MCM2$^-$] NSCs). Scale bars: 50 μm (left panels) and 20 μm (middle panels). Cumulative frequency distribution plots of OPP mean intensity (right panel) in dividing NSCs (red line) and quiescent NSCs (black line). ($n > 300$ cells; $^*p < 0.05$; $^{**}p < 0.01$; Kolmogorov-Smirnov test).

(G) Cumulative frequency distribution plot of OPP mean intensity in quiescent (HOPX$^+$MCM2$^-$) NSCs at P7 (purple line) and P14 (blue line). Same data in (E) and (F) are replotted ($^{****}p < 0.0001$; Kolmogorov-Smirnov test).

Also see Figure S4 and Tables S2 and S3.

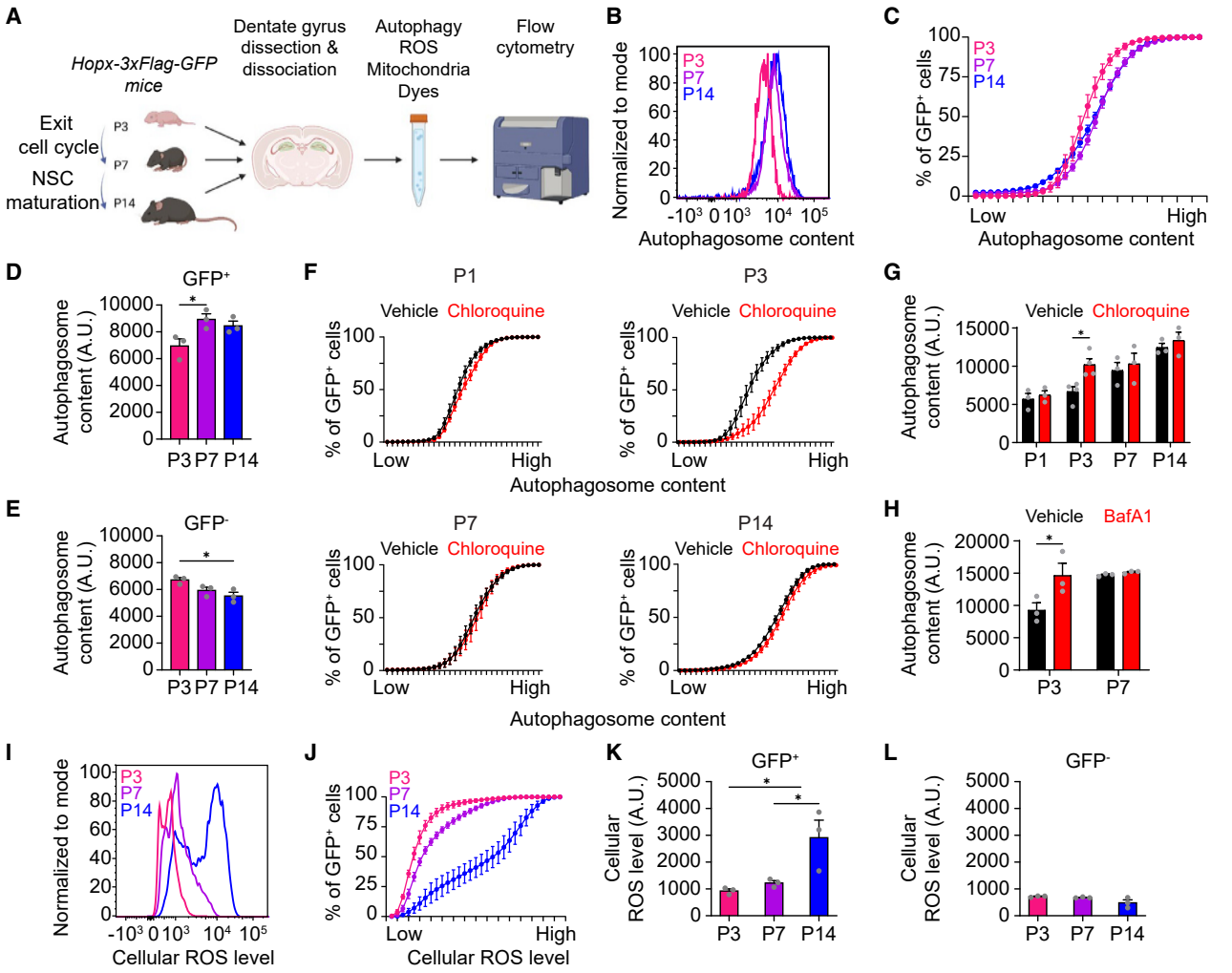

Figure 5. Targeted metabolic analysis reveals distinct changes in autophagy and ROS in NSCs during the transition to a quiescent adult state

(A) Diagram of metabolic analysis workflow. DG cells were isolated from *Hopx-3xFlag-GFP* mice at P3, P7, and P14 and loaded with dyes to measure autophagic vesicle content, cellular reactive oxygen species (ROS), and mitochondrial mass in via flow cytometry.

(B–E) Flow cytometry analysis of autophagic vesicle content in GFP$^+$ cells (B–D) and GFP$^-$ cells (E) using Autophagy Assay Kit (Red) shown as a histogram plot of individual samples (B), a cumulative distribution plot of all samples (C), and a bar plot of the average of all samples (D and E; individual dots represent data from each experiment). Values represent mean ± SEM (n = 3 experiments; 3 mice were pooled for each experimental sample; *p < 0.05; one-way ANOVA with Tukey's post hoc test).

(F and G) Flow cytometry analysis of autophagic vesicle content in GFP$^+$ cells after vehicle or chloroquine (10 μM) treatment shown as a cumulative distribution plot of all samples (F) and as a bar plot of the average of all samples (G). Values represent mean ± SEM (n = 3 experiments; 3 mice were pooled for each experimental sample; *p < 0.05; two-way ANOVA with Šídák's multiple comparisons test).

(H) Bar plot of flow cytometry analysis of autophagic vesicle content in GFP$^+$ cells after vehicle or bafilomycin A (BafA1; 10 nM) treatment. Values represent mean ± SEM (n = 3 experiments; 3 mice were pooled for each experimental sample; *p < 0.05; two-way ANOVA with Šídák's multiple comparisons test).

(I–L) Flow cytometry analysis of cellular ROS levels in GFP$^+$ cells (I–K) and GFP$^-$ cells (L) using dihydroethidium (DHE). Similar as in (B)–(E). Values represent mean ± SEM (n = 3 experiments; 3 mice were pooled for each experimental sample; *p < 0.05; one-way ANOVA with Tukey's post hoc test).

Also see Figure S5.

presence of a long-lived, quiescent NSC population. Accumulating evidence demonstrates that the protracted nature of DG development and the order of developmental milestones is conserved between species, despite differences in the timing.[16,84,85,97,102–111] Thus, the relative timing of milestones in rodents could be used as a guide for studying human DG development. For example, the establishment of a long-lived, quiescent NSC population in the mouse DG occurs immediately following peak neurogenesis,[107] and peak neurogenesis occurs during mid-gestation in the human DG.[97,104,105] Future work investigating human DG NSC development during the fetal period will be essential to understanding the potential for lifelong human neurogenesis.

While this study focused on stem cells in the brain, many organs in the body harbor a population of adult stem cells, and the principles identified here may apply broadly to the

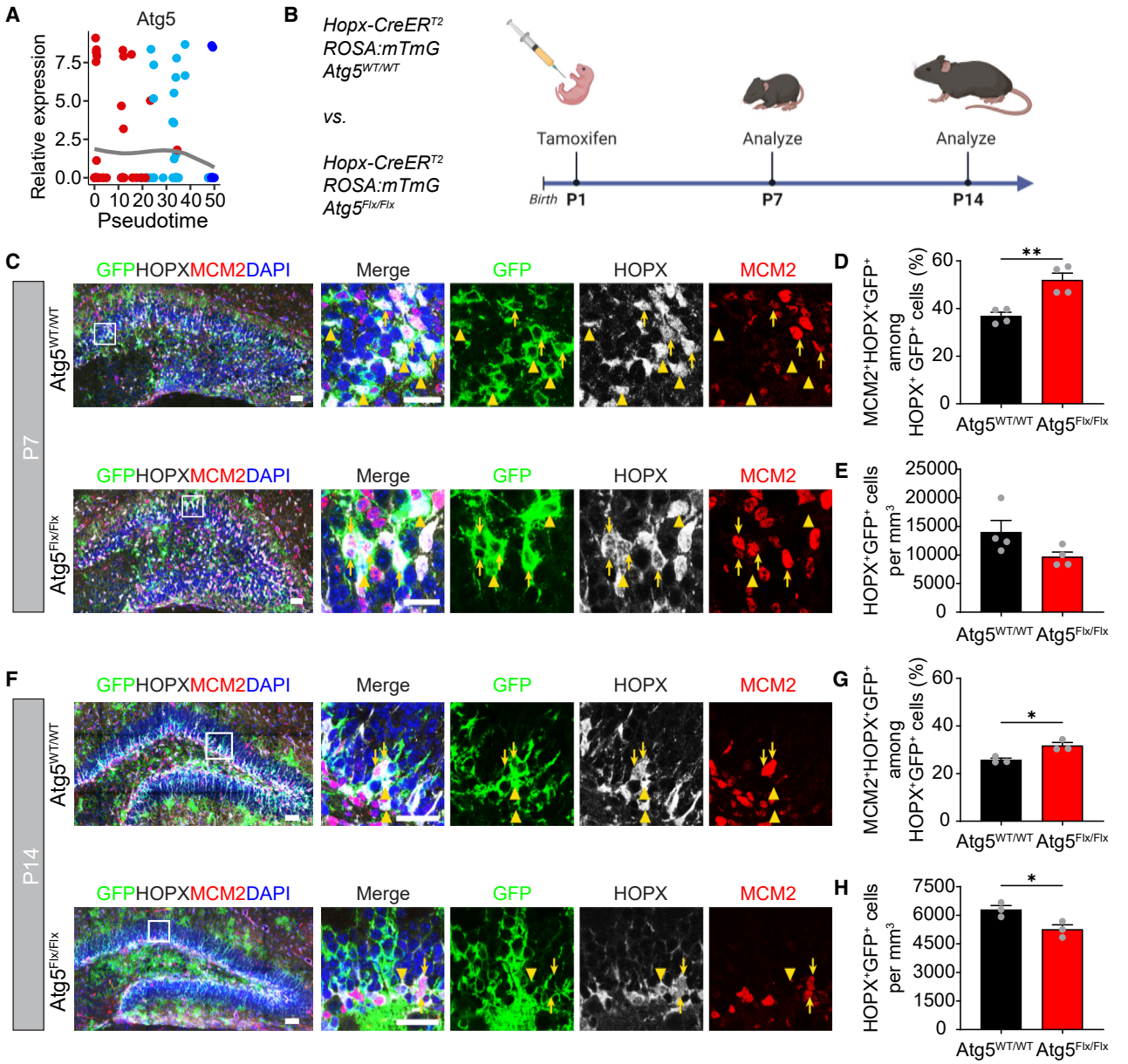

Figure 6. Blocking autophagy attenuates the NSC transition to quiescence

(A) Dot plot of *Atg5* gene expression across the pseudotime (Figure 2D).

(B) Experimental paradigm to knock out *Atg5* in DG NSCs *in vivo*. *Hopx-CreER^{T2}::mTmG Atg5$^{wt/wt}$* and *Hopx-CreER^{T2}::mTmG Atg5$^{Flx/Flx}$* mice were administered tamoxifen at P1 and analyzed at P7 and P14.

(C) Sample confocal images of GFP$^+$HOPX$^+$ cells in the DG at P7 in *Hopx-CreER^{T2}::mTmG Atg5$^{wt/wt}$* and *Hopx-CreER^{T2}::mTmG Atg5$^{Flx/Flx}$* mice (left panels). Boxed area is shown at higher magnification (right panels) to view GFP$^+$HOPX$^+$MCM2$^+$ cells (arrows) and GFP$^+$HOPX$^+$MCM2$^-$ cells (arrowheads). Scale bars, 50 μm (left panels) and 25 μm (right panels).

(D) Quantification of the percentage of MCM2$^+$ cells among all GFP$^+$HOPX$^+$ cells in the DG at P7. Each dot represents data from one mouse. Values represent mean ± SEM (n = 4 mice; $^{**}p < 0.01$; unpaired t test).

(E) Quantification of the number of GFP$^+$HOPX$^+$ cells in the DG at P7. Each dot represents data from one mouse. Values represent mean ± SEM (n = 4 mice).

(F) Sample confocal images of GFP$^+$HOPX$^+$ cells in the DG at P14 in *Hopx-CreER^{T2}::mTmG Atg5$^{wt/wt}$* and *Hopx-CreER^{T2}::mTmG Atg5$^{Flx/Flx}$* mice (left panels). Boxed area is shown at higher magnification (right panels) to view GFP$^+$HOPX$^+$MCM2$^+$ cells (arrows) and GFP$^+$HOPX$^+$MCM2$^-$ cells (arrowheads). Scale bars, 50 μm (left panels) and 25 μm (right panels).

(legend continued on next page)

developmental establishment of other somatic stem cell populations. Many studies have identified the developmental origins of hematopoietic stem cells,[112] muscle stem cells (satellite cells),[113–115] and intestinal stem cells,[116] but the process(es) leading to the establishment of the adult stem cell state remains largely unclear. Our study presents a methodological outline to approach the study of stem cell development in other systems. An unrealized feature of many somatic stem cell populations is that quiescence acquisition is not coupled to the establishment of the adult stem cell state. For example, SVZ NSCs become quiescent embryonically[21,22] but do not acquire an adult molecular signature or localization to the center of a pinwheel structure until after birth.[77,117] Similarly, a significant proportion of muscle stem cells become quiescent before they acquire satellite cell characteristics and locate to their adult niche under the basal lamina.[118] Hematopoietic stem cells colonize the bone marrow niche as early as E16.5 in mice[119] but do not acquire an adult molecular signature, long-term repopulating activity, or quiescence until after birth.[120,121] What drives stem cell maturation into an adult state remains largely unknown, but our work suggests that it may be driven by changes in stem cell metabolism.[18] Distinct metabolic changes occur as quiescent adult stem cells reactivate, and many of these changes are common across systems.[19,33] For example, quiescent adult stem cells have low levels of transcription and translation that get upregulated with activation.[122–125] Additionally, quiescent adult stem cells have increased heterochromatin and lower chromatin accessibility, which is reversed upon activation.[126–128] Many previous studies have suggested that adult quiescent stem cells rely on glycolysis as their primary energy source but switch to mitochondrial respiration upon activation.[129–133] However, recent studies demonstrate a more prominent role for mitochondrial activity during quiescence,[37,134] suggesting that there is still a lot to learn about the relationship between metabolism and stem cell function. Future work will benefit from comparisons between systems, given the potential for common mechanisms to establish and maintain adult stem cell pools. Detailed time course analyses across embryonic and postnatal development will be required to better delineate different phases of stem cell development and to uncover both common and tissue-specific mechanisms regulating the establishment of adult stem cell populations.

Limitations of the study

First, this study focused on the intrinsic properties of DG NSCs and did not investigate extrinsic changes in the environment that may influence the establishment of the adult NSC pool. There are undoubtedly changes in the signaling environment during this dynamic period of early postnatal development,[30,107] and future studies should investigate how these changes impact NSC development. Second, our study was designed based on previous knowledge that by the end of the second postnatal week the majority (>80%) of NSCs have shifted to quiescence,[16] and the SGZ niche resembles its adult form.[25] Previous studies have demonstrated changes in NSC behavior across adulthood[14,82]; therefore, it is likely that additional changes occur to the NSCs after P14. Third, our scRNA-seq data demonstrate the heterogeneity of the *Hopx*$^+$ population, which could not be controlled for in the rest of our experiments. Future experiments could use index sorting to link transcriptomic and metabolic data at the single-cell level. Finally, though we tested the causality of autophagy in regulating the establishment of the quiescent adult NSC state, we did not test the causality of other milestones, like cellular ROS. Future studies could determine whether other milestones identified here are drivers of NSC development.

In summary, our deliberate and comprehensive investigation of the establishment of the quiescent adult NSC pool in the DG demonstrates that acquisition of the adult NSC state is not simply a switch from proliferation to quiescence but is instead a progressive process. Many somatic stem cell populations undergo a similar developmental process to establish their quiescent adult stem cell pools, and our study identifies a framework that may be universal across systems. Further detailed study of the developmental process that establishes adult stem cell pools will be critical to understanding the body's capacity for lifelong plasticity and regeneration.

STAR★METHODS

Detailed methods are provided in the online version of this paper and include the following:

- KEY RESOURCES TABLE
- RESOURCE AVAILABILITY
  - Lead contact
  - Materials availability
  - Data and code availability
- EXPERIMENTAL MODEL AND STUDY PARTICIPANT DETAILS
  - Animals
- METHOD DETAILS
  - Tissue processing and immunohistology
  - Confocal microscopy and image processing
  - Single-cell RNA-sequencing
  - Single-cell RNA-sequencing analyses
  - Measuring global translation levels with OPP incorporation
  - Primary cortical astrocyte culture
  - Flow cytometry and analysis
  - Tamoxifen injection
- QUANTIFICATION AND STATISTICAL ANALYSIS

SUPPLEMENTAL INFORMATION

Supplemental information can be found online at https://doi.org/10.1016/j.celrep.2024.114339.

ACKNOWLEDGMENTS

We thank members of the Ming and Song laboratories for comments and suggestions and B. Temsamrit, E. LaNoce, G. Alepa, and A. Angelucci for

(G) Quantification of the percentage of MCM2$^+$ cells among all GFP$^+$HOPX$^+$ cells in the DG at P14. Each dot represents data from one mouse. Values represent mean ± SEM (n = 4 mice; *p < 0.05; unpaired t test).
(H) Quantification of the number of GFP$^+$HOPX$^+$ cells in the DG at P14. Each dot represents data from one mouse. Values represent mean ± SEM (n = 4 mice; *p < 0.05; unpaired t test).
Also see Figure S6.

laboratory support. This work was supported by grants from the National Institutes of Health (R01NS110716 to S.M., R35NS097370 to G.-l.M., R35NS116843 to H.S., and K01MH125144 to A.M.B.) and from Dr. Miriam and Sheldon G. Adelson Medical Research Foundation (to G.-l.M.). Some figures were created with BioRender.com.

AUTHOR CONTRIBUTIONS

Conceptualization: G.-l.M., H.S., and A.M.B.; bioinformatics: D.J.-C.; data analysis: D.J.-C., V.S.A., and A.M.B.; data acquisition: D.J.-C., V.S.A., M.H.S., and A.M.B.; resources: S.M.; data curation: D.J.-C.; writing – original draft: A.M.B.; writing – review & editing: D.J.-C., V.S.A., M.H.S., S.M., G.-l.M., H.S., and A.M.B.; visualization: D.J.-C., V.S.A., G.-l.M., and A.M.B.; supervision: S.M., G.-l.M., H.S., and A.M.B.; funding support: S.M., G.-l.M., H.S., and A.M.B.

DECLARATION OF INTERESTS

The authors declare no other competing interests.

Received: May 27, 2023
Revised: April 16, 2024
Accepted: May 23, 2024
Published: June 8, 2024

REFERENCES

1. Gage, F.H. (2019). Adult neurogenesis in mammals. Science *364*, 827–828. https://doi.org/10.1126/science.aav6885.
2. Bond, A.M., Ming, G.L., and Song, H. (2015). Adult Mammalian Neural Stem Cells and Neurogenesis: Five Decades Later. Cell Stem Cell *17*, 385–395. https://doi.org/10.1016/j.stem.2015.09.003.
3. Ming, G.L., and Song, H. (2011). Adult Neurogenesis in the Mammalian Brain: Significant Answers and Significant Questions. Neuron *70*, 687–702. https://doi.org/10.1016/j.neuron.2011.05.001.
4. Christian, K.M., Song, H., and Ming, G.l. (2014). Functions and Dysfunctions of Adult Hippocampal Neurogenesis. Annu. Rev. Neurosci. *37*, 243–262. https://doi.org/10.1146/annurev-neuro-071013-014134.
5. Anacker, C., and Hen, R. (2017). Adult hippocampal neurogenesis and cognitive flexibility — linking memory and mood. Nat. Rev. Neurosci. *18*, 335–346. https://doi.org/10.1038/nrn.2017.45.
6. Miller, S.M., and Sahay, A. (2019). Functions of adult-born neurons in hippocampal memory interference and indexing. Nat. Neurosci. *22*, 1565–1575. https://doi.org/10.1038/s41593-019-0484-2.
7. Toda, T., Parylak, S.L., Linker, S.B., and Gage, F.H. (2019). The role of adult hippocampal neurogenesis in brain health and disease. Mol. Psychiatr. *24*, 67–87. https://doi.org/10.1038/s41380-018-0036-2.
8. Berger, T., Lee, H., Young, A.H., Aarsland, D., and Thuret, S. (2020). Adult Hippocampal Neurogenesis in Major Depressive Disorder and Alzheimer's Disease. Trends Mol. Med. *26*, 803–818. https://doi.org/10.1016/j.molmed.2020.03.010.
9. Bielefeld, P., Durá, I., Danielewicz, J., Lucassen, P.J., Baekelandt, V., Abrous, D.N., Encinas, J.M., and Fitzsimons, C.P. (2019). Insult-induced aberrant hippocampal neurogenesis: Functional consequences and possible therapeutic strategies. Behav. Brain Res. *372*, 112032. https://doi.org/10.1016/j.bbr.2019.112032.
10. Jessberger, S., and Parent, J.M. (2015). Epilepsy and Adult Neurogenesis. Cold Spring Harbor Perspect. Biol. *7*, a020677. https://doi.org/10.1101/cshperspect.a020677.
11. Kuhn, H.G., Dickinson-Anson, H., and Gage, F.H. (1996). Neurogenesis in the dentate gyrus of the adult rat: age-related decrease of neuronal progenitor proliferation. J. Neurosci. *16*, 2027–2033. https://doi.org/10.1523/JNEUROSCI.16-06-02027.1996.
12. Ben Abdallah, N.M.-B., Slomianka, L., Vyssotski, A.L., and Lipp, H.-P. (2010). Early age-related changes in adult hippocampal neurogenesis in C57 mice. Neurobiol. Aging *31*, 151–161. https://doi.org/10.1016/j.neurobiolaging.2008.03.002.
13. Encinas, J.M., Michurina, T.V., Peunova, N., Park, J.-H., Tordo, J., Peterson, D.A., Fishell, G., Koulakov, A., and Enikolopov, G. (2011). Division-Coupled Astrocytic Differentiation and Age-Related Depletion of Neural Stem Cells in the Adult Hippocampus. Cell Stem Cell *8*, 566–579. https://doi.org/10.1016/j.stem.2011.03.010.
14. Ibrayeva, A., Bay, M., Pu, E., Jörg, D.J., Peng, L., Jun, H., Zhang, N., Aaron, D., Lin, C., Resler, G., et al. (2021). Early stem cell aging in the mature brain. Cell Stem Cell *28*, 955–966.e7. https://doi.org/10.1016/j.stem.2021.03.018.
15. Li, G., Fang, L., Fernández, G., and Pleasure, S.J. (2013). The Ventral Hippocampus Is the Embryonic Origin for Adult Neural Stem Cells in the Dentate Gyrus. Neuron *78*, 658–672. https://doi.org/10.1016/j.neuron.2013.03.019.
16. Berg, D.A., Su, Y., Jimenez-Cyrus, D., Patel, A., Huang, N., Morizet, D., Lee, S., Shah, R., Ringeling, F.R., Jain, R., et al. (2019). A Common Embryonic Origin of Stem Cells Drives Developmental and Adult Neurogenesis. Cell *177*, 654–668.e15. https://doi.org/10.1016/j.cell.2019.02.010.
17. Zhang, F., Yoon, K., Kim, N.-S., Ming, G.L., and Song, H. (2023). Cell-autonomous and non-cell-autonomous roles of NKCC1 in regulating neural stem cell quiescence in the hippocampal dentate gyrus. Stem Cell Rep. *18*, 1468–1481. https://doi.org/10.1016/j.stemcr.2023.05.021.
18. Calatayud-Baselga, I., Casares-Crespo, L., Franch-Ibáñez, C., Guijarro-Nuez, J., Sanz, P., and Mira, H. (2023). Autophagy drives the conversion of developmental neural stem cells to the adult quiescent state. Nat. Commun. *14*, 7541. https://doi.org/10.1038/s41467-023-43222-1.
19. van Velthoven, C.T.J., and Rando, T.A. (2019). Stem Cell Quiescence: Dynamism, Restraint, and Cellular Idling. Cell Stem Cell *24*, 213–225. https://doi.org/10.1016/j.stem.2019.01.001.
20. Urbán, N., Blomfield, I.M., and Guillemot, F. (2019). Quiescence of Adult Mammalian Neural Stem Cells: A Highly Regulated Rest. Neuron *104*, 834–848. https://doi.org/10.1016/j.neuron.2019.09.026.
21. Fuentealba, L.C., Rompani, S.B., Parraguez, J.I., Obernier, K., Romero, R., Cepko, C.L., and Alvarez-Buylla, A. (2015). Embryonic Origin of Postnatal Neural Stem Cells. Cell *161*, 1644–1655. https://doi.org/10.1016/j.cell.2015.05.041.
22. Furutachi, S., Miya, H., Watanabe, T., Kawai, H., Yamasaki, N., Harada, Y., Imayoshi, I., Nelson, M., Nakayama, K.I., Hirabayashi, Y., and Gotoh, Y. (2015). Slowly dividing neural progenitors are an embryonic origin of adult neural stem cells. Nat. Neurosci. *18*, 657–665. https://doi.org/10.1038/nn.3989.
23. Brunne, B., Zhao, S., Derouiche, A., Herz, J., May, P., Frotscher, M., and Bock, H.H. (2010). Origin, maturation, and astroglial transformation of secondary radial glial cells in the developing dentate gyrus. Glia *58*, 1553–1569. https://doi.org/10.1002/glia.21029.
24. Seki, T., Sato, T., Toda, K., Osumi, N., Imura, T., and Shioda, S. (2014). Distinctive population of Gfap-expressing neural progenitors arising around the dentate notch migrate and form the granule cell layer in the developing hippocampus. J. Comp. Neurol. *522*, 261–283. https://doi.org/10.1002/cne.23460.
25. Nicola, Z., Fabel, K., and Kempermann, G. (2015). Development of the adult neurogenic niche in the hippocampus of mice. Front. Neuroanat. *9*, 53.
26. Gilley, J.A., Yang, C.-P., and Kernie, S.G. (2011). Developmental profiling of postnatal dentate gyrus progenitors provides evidence for dynamic cell-autonomous regulation. Hippocampus *21*, 33–47. https://doi.org/10.1002/hipo.20719.
27. Bonaguidi, M.A., Wheeler, M.A., Shapiro, J.S., Stadel, R.P., Sun, G.J., Ming, G.l., and Song, H. (2011). In Vivo Clonal Analysis Reveals

Self-Renewing and Multipotent Adult Neural Stem Cell Characteristics. Cell *145*, 1142–1155. https://doi.org/10.1016/j.cell.2011.05.024.

28. Namba, T., Mochizuki, H., Suzuki, R., Onodera, M., Yamaguchi, M., Namiki, H., Shioda, S., and Seki, T. (2011). Time-Lapse Imaging Reveals Symmetric Neurogenic Cell Division of GFAP-Expressing Progenitors for Expansion of Postnatal Dentate Granule Neurons. PLoS One *6*, e25303. https://doi.org/10.1371/journal.pone.0025303.
29. Pilz, G.-A., Bottes, S., Betizeau, M., Jörg, D.J., Carta, S., April, S., Simons, B.D., Helmchen, F., and Jessberger, S. (2018). Live imaging of neurogenesis in the adult mouse hippocampus. Science *359*, 658–662. https://doi.org/10.1126/science.aao5056.
30. Bond, A.M., Ming, G., and Song, H. (2021). Chapter Two - Ontogeny of adult neural stem cells in the mammalian brain. In Current Topics in Developmental Biology Molecular Mechanisms of Neural Development and Insights into Disease, G.J. Bashaw, ed. (Academic Press), pp. 67–98. https://doi.org/10.1016/bs.ctdb.2020.11.002.
31. Hochgerner, H., Zeisel, A., Lönnerberg, P., and Linnarsson, S. (2018). Conserved properties of dentate gyrus neurogenesis across postnatal development revealed by single-cell RNA sequencing. Nat. Neurosci. *21*, 290–299. https://doi.org/10.1038/s41593-017-0056-2.
32. Ly, C.H., Lynch, G.S., and Ryall, J.G. (2020). A Metabolic Roadmap for Somatic Stem Cell Fate. Cell Metabol. *31*, 1052–1067. https://doi.org/10.1016/j.cmet.2020.04.022.
33. de Morree, A., and Rando, T.A. (2023). Regulation of adult stem cell quiescence and its functions in the maintenance of tissue integrity. Nat. Rev. Mol. Cell Biol. *24*, 334–354. https://doi.org/10.1038/s41580-022-00568-6.
34. Shin, J., Berg, D.A., Zhu, Y., Shin, J.Y., Song, J., Bonaguidi, M.A., Enikolopov, G., Nauen, D.W., Christian, K.M., Ming, G.l., and Song, H. (2015). Single-Cell RNA-Seq with Waterfall Reveals Molecular Cascades underlying Adult Neurogenesis. Cell Stem Cell *17*, 360–372. https://doi.org/10.1016/j.stem.2015.07.013.
35. Leeman, D.S., Hebestreit, K., Ruetz, T., Webb, A.E., McKay, A., Pollina, E.A., Dulken, B.W., Zhao, X., Yeo, R.W., Ho, T.T., et al. (2018). Lysosome activation clears aggregates and enhances quiescent neural stem cell activation during aging. Science *359*, 1277–1283. https://doi.org/10.1126/science.aag3048.
36. Knobloch, M., Braun, S.M.G., Zurkirchen, L., von Schoultz, C., Zamboni, N., Araúzo-Bravo, M.J., Kovacs, W.J., Karalay, O., Suter, U., Machado, R.A.C., et al. (2013). Metabolic control of adult neural stem cell activity by Fasn-dependent lipogenesis. Nature *493*, 226–230. https://doi.org/10.1038/nature11689.
37. Petrelli, F., Scandella, V., Montessuit, S., Zamboni, N., Martinou, J.-C., and Knobloch, M. (2023). Mitochondrial pyruvate metabolism regulates the activation of quiescent adult neural stem cells. Sci. Adv. *9*, eadd5220. https://doi.org/10.1126/sciadv.add5220.
38. Knobloch, M., Pilz, G.-A., Ghesquière, B., Kovacs, W.J., Wegleiter, T., Moore, D.L., Hruzova, M., Zamboni, N., Carmeliet, P., and Jessberger, S. (2017). A Fatty Acid Oxidation-Dependent Metabolic Shift Regulates Adult Neural Stem Cell Activity. Cell Rep. *20*, 2144–2155. https://doi.org/10.1016/j.celrep.2017.08.029.
39. Takeda, N., Jain, R., LeBoeuf, M.R., Padmanabhan, A., Wang, Q., Li, L., Lu, M.M., Millar, S.E., and Epstein, J.A. (2013). Hopx expression defines a subset of multipotent hair follicle stem cells and a progenitor population primed to give rise to K6+ niche cells. Development *140*, 1655–1664. https://doi.org/10.1242/dev.093005.
40. Williams, G.H., and Stoeber, K. (2007). Cell cycle markers in clinical oncology. Curr. Opin. Cell Biol. *19*, 672–679. https://doi.org/10.1016/j.ceb.2007.10.005.
41. Stoeber, K., Tlsty, T.D., Happerfield, L., Thomas, G.A., Romanov, S., Bobrow, L., Williams, E.D., and Williams, G.H. (2001). DNA replication licensing and human cell proliferation. J. Cell Sci. *114*, 2027–2041. https://doi.org/10.1242/jcs.114.11.2027.
42. McGarry, T.J., and Kirschner, M.W. (1998). Geminin, an Inhibitor of DNA Replication, Is Degraded during Mitosis. Cell *93*, 1043–1053. https://doi.org/10.1016/S0092-8674(00)81209-X.
43. Picelli, S., Faridani, O.R., Björklund, A.K., Winberg, G., Sagasser, S., and Sandberg, R. (2014). Full-length RNA-seq from single cells using Smart-seq2. Nat. Protoc. *9*, 171–181. https://doi.org/10.1038/nprot.2014.006.
44. Li, D., Takeda, N., Jain, R., Manderfield, L.J., Liu, F., Li, L., Anderson, S.A., and Epstein, J.A. (2015). Hopx distinguishes hippocampal from lateral ventricle neural stem cells. Stem Cell Res. *15*, 522–529. https://doi.org/10.1016/j.scr.2015.09.015.
45. Batiuk, M.Y., Martirosyan, A., Wahis, J., de Vin, F., Marneffe, C., Kusserow, C., Koeppen, J., Viana, J.F., Oliveira, J.F., Voet, T., et al. (2020). Identification of region-specific astrocyte subtypes at single cell resolution. Nat. Commun. *11*, 1220. https://doi.org/10.1038/s41467-019-14198-8.
46. La Manno, G., Soldatov, R., Zeisel, A., Braun, E., Hochgerner, H., Petukhov, V., Lidschreiber, K., Kastriti, M.E., Lönnerberg, P., Furlan, A., et al. (2018). RNA velocity of single cells. Nature *560*, 494–498. https://doi.org/10.1038/s41586-018-0414-6.
47. Wang, Y., Lin, L., Lai, H., Parada, L.F., and Lei, L. (2013). Transcription factor Sox11 is essential for both embryonic and adult neurogenesis. Dev. Dynam. *242*, 638–653. https://doi.org/10.1002/dvdy.23962.
48. Miller, J.A., Nathanson, J., Franjic, D., Shim, S., Dalley, R.A., Shapouri, S., Smith, K.A., Sunkin, S.M., Bernard, A., Bennett, J.L., et al. (2013). Conserved molecular signatures of neurogenesis in the hippocampal subgranular zone of rodents and primates. Development *140*, 4633–4644. https://doi.org/10.1242/dev.097212.
49. Heng, Y.H.E., McLeay, R.C., Harvey, T.J., Smith, A.G., Barry, G., Cato, K., Plachez, C., Little, E., Mason, S., Dixon, C., et al. (2014). NFIX Regulates Neural Progenitor Cell Differentiation During Hippocampal Morphogenesis. Cerebr. Cortex *24*, 261–279. https://doi.org/10.1093/cercor/bhs307.
50. Kamnasaran, D., Muir, W.J., Ferguson-Smith, M.A., and Cox, D.W. (2003). Disruption of the neuronal PAS3 gene in a family affected with schizophrenia. J. Med. Genet. *40*, 325–332. https://doi.org/10.1136/jmg.40.5.325.
51. Pickard, B.S., Malloy, M.p., Porteous, D.j., Blackwood, D.h. r., and Muir, W.j. (2005). Disruption of a brain transcription factor, NPAS3, is associated with schizophrenia and learning disability. Am. J. Med. Genet. B Neuropsychiatr. Genet. *136B*, 26–32. https://doi.org/10.1002/ajmg.b.30204.
52. Rossi, J.J., Rosenfeld, J.A., Chan, K.M., Streff, H., Nankivell, V., Peet, D.J., Whitelaw, M.L., and Bersten, D.C. (2021). Molecular characterisation of rare loss-of-function NPAS3 and NPAS4 variants identified in individuals with neurodevelopmental disorders. Sci. Rep. *11*, 6602. https://doi.org/10.1038/s41598-021-86041-4.
53. Pieper, A.A., Wu, X., Han, T.W., Estill, S.J., Dang, Q., Wu, L.C., Reece-Fincanon, S., Dudley, C.A., Richardson, J.A., Brat, D.J., and McKnight, S.L. (2005). The neuronal PAS domain protein 3 transcription factor controls FGF-mediated adult hippocampal neurogenesis in mice. Proc. Natl. Acad. Sci. USA *102*, 14052–14057. https://doi.org/10.1073/pnas.0506713102.
54. Lehnertz, B., Chagraoui, J., MacRae, T., Tomellini, E., Corneau, S., Mayotte, N., Boivin, I., Durand, A., Gracias, D., and Sauvageau, G. (2021). HLF expression defines the human hematopoietic stem cell state. Blood *138*, 2642–2654. https://doi.org/10.1182/blood.2021010745.
55. Komorowska, K., Doyle, A., Wahlestedt, M., Subramaniam, A., Debnath, S., Chen, J., Soneji, S., Van Handel, B., Mikkola, H.K.A., Miharada, K., et al. (2017). Hepatic Leukemia Factor Maintains Quiescence of Hematopoietic Stem Cells and Protects the Stem Cell Pool during Regeneration. Cell Rep. *21*, 3514–3523. https://doi.org/10.1016/j.celrep.2017.11.084.
56. Tang, W., He, J., Huang, T., Bai, Z., Wang, C., Wang, H., Yang, R., Ni, Y., Hou, J., Wang, J., et al. (2021). Hlf Expression Marks Early Emergence of

Hematopoietic Stem Cell Precursors With Adult Repopulating Potential and Fate. Front. Cell Dev. Biol. *9*, 728057.

57. Lummertz da Rocha, E., Rowe, R.G., Lundin, V., Malleshaiah, M., Jha, D.K., Rambo, C.R., Li, H., North, T.E., Collins, J.J., and Daley, G.Q. (2018). Reconstruction of complex single-cell trajectories using CellRouter. Nat. Commun. *9*, 892. https://doi.org/10.1038/s41467-018-03214-y.
58. Chang, N.C. (2020). Autophagy and Stem Cells: Self-Eating for Self-Renewal. Front. Cell Dev. Biol. *8*, 138.
59. Murley, A., and Dillin, A. (2023). Macroautophagy in quiescent and senescent cells: a pathway to longevity? Trends Cell Biol. *33*, 495–504. https://doi.org/10.1016/j.tcb.2022.10.004.
60. Wang, C., Liang, C.-C., Bian, Z.C., Zhu, Y., and Guan, J.-L. (2013). FIP200 is required for maintenance and differentiation of postnatal neural stem cells. Nat. Neurosci. *16*, 532–542. https://doi.org/10.1038/nn.3365.
61. Yazdankhah, M., Farioli-Vecchioli, S., Tonchev, A.B., Stoykova, A., and Cecconi, F. (2014). The autophagy regulators Ambra1 and Beclin 1 are required for adult neurogenesis in the brain subventricular zone. Cell Death Dis. *5*, e1403. https://doi.org/10.1038/cddis.2014.358.
62. Xi, Y., Dhaliwal, J.S., Ceizar, M., Vaculik, M., Kumar, K.L., and Lagace, D.C. (2016). Knockout of Atg5 delays the maturation and reduces the survival of adult-generated neurons in the hippocampus. Cell Death Dis. *7*, e2127. https://doi.org/10.1038/cddis.2015.406.
63. Williams, P.A., Parham, L.R., Acheampong, K.K., Danan, C.H., Ma, X., Simon, L.A., Naughton, K.E., Karakasheva, T., Whelan, K.A., Brady, D.C., et al. (2022). IGF2BP1/IMP1 contributes to autophagy modulation directly via MAP1LC3B. Preprint at bioRxiv. https://doi.org/10.1101/2022.02.28.482365.
64. Mizushima, N., Yamamoto, A., Matsui, M., Yoshimori, T., and Ohsumi, Y. (2004). In vivo analysis of autophagy in response to nutrient starvation using transgenic mice expressing a fluorescent autophagosome marker. Mol. Biol. Cell *15*, 1101–1111. https://doi.org/10.1091/mbc.e03-09-0704.
65. Kuma, A., Hatano, M., Matsui, M., Yamamoto, A., Nakaya, H., Yoshimori, T., Ohsumi, Y., Tokuhisa, T., and Mizushima, N. (2004). The role of autophagy during the early neonatal starvation period. Nature *432*, 1032–1036. https://doi.org/10.1038/nature03029.
66. Dong, A., Kulkarni, V.V., and Maday, S. (2019). Methods for Imaging Autophagosome Dynamics in Primary Neurons. In Autophagy: Methods and Protocols Methods in Molecular Biology, N. Ktistakis and O. Florey, eds. (Springer), pp. 243–256. https://doi.org/10.1007/978-1-4939-8873-0_16.
67. Moulis, M., and Vindis, C. (2017). Methods for Measuring Autophagy in Mice. Cells *6*, 14. https://doi.org/10.3390/cells6020014.
68. du Toit, A., Hofmeyr, J.-H.S., Gniadek, T.J., and Loos, B. (2018). Measuring autophagosome flux. Autophagy *14*, 1060–1071. https://doi.org/10.1080/15548627.2018.1469590.
69. Sinenko, S.A., Starkova, T.Y., Kuzmin, A.A., and Tomilin, A.N. (2021). Physiological Signaling Functions of Reactive Oxygen Species in Stem Cells: From Flies to Man. Front. Cell Dev. Biol. *9*, 714370.
70. Ye, Z.-W., Zhang, J., Townsend, D.M., and Tew, K.D. (2015). Oxidative stress, redox regulation and diseases of cellular differentiation. Biochim. Biophys. Acta *1850*, 1607–1621. https://doi.org/10.1016/j.bbagen.2014.11.010.
71. Holmström, K.M., and Finkel, T. (2014). Cellular mechanisms and physiological consequences of redox-dependent signalling. Nat. Rev. Mol. Cell Biol. *15*, 411–421. https://doi.org/10.1038/nrm3801.
72. Adusumilli, V.S., Walker, T.L., Overall, R.W., Klatt, G.M., Zeidan, S.A., Zocher, S., Kirova, D.G., Ntitsias, K., Fischer, T.J., Sykes, A.M., et al. (2021). ROS Dynamics Delineate Functional States of Hippocampal Neural Stem Cells and Link to Their Activity-Dependent Exit from Quiescence. Cell Stem Cell *28*, 300–314.e6. https://doi.org/10.1016/j.stem.2020.10.019.
73. Khacho, M., Harris, R., and Slack, R.S. (2019). Mitochondria as central regulators of neural stem cell fate and cognitive function. Nat. Rev. Neurosci. *20*, 34–48. https://doi.org/10.1038/s41583-018-0091-3.
74. Zorov, D.B., Juhaszova, M., and Sollott, S.J. (2014). Mitochondrial Reactive Oxygen Species (ROS) and ROS-Induced ROS Release. Physiol. Rev. *94*, 909–950. https://doi.org/10.1152/physrev.00026.2013.
75. Lugli, E., Troiano, L., Ferraresi, R., Roat, E., Prada, N., Nasi, M., Pinti, M., Cooper, E.L., and Cossarizza, A. (2005). Characterization of cells with different mitochondrial membrane potential during apoptosis. Cytometry A. *68*, 28–35. https://doi.org/10.1002/cyto.a.20188.
76. Hara, T., Nakamura, K., Matsui, M., Yamamoto, A., Nakahara, Y., Suzuki-Migishima, R., Yokoyama, M., Mishima, K., Saito, I., Okano, H., and Mizushima, N. (2006). Suppression of basal autophagy in neural cells causes neurodegenerative disease in mice. Nature *441*, 885–889. https://doi.org/10.1038/nature04724.
77. Borrett, M.J., Innes, B.T., Jeong, D., Tahmasian, N., Storer, M.A., Bader, G.D., Kaplan, D.R., and Miller, F.D. (2020). Single-Cell Profiling Shows Murine Forebrain Neural Stem Cells Reacquire a Developmental State when Activated for Adult Neurogenesis. Cell Rep. *32*, 108022. https://doi.org/10.1016/j.celrep.2020.108022.
78. Guo, N., McDermott, K.D., Shih, Y.-T., Zanga, H., Ghosh, D., Herber, C., Meara, W.R., Coleman, J., Zagouras, A., Wong, L.P., et al. (2022). Transcriptional regulation of neural stem cell expansion in the adult hippocampus. Elife *11*, e72195. https://doi.org/10.7554/eLife.72195.
79. Falini, B., Brunetti, L., Sportoletti, P., and Martelli, M.P. (2020). NPM1-mutated acute myeloid leukemia: from bench to bedside. Blood *136*, 1707–1721. https://doi.org/10.1182/blood.2019004226.
80. Morganti, C., Ito, K., Yanase, C., Verma, A., Teruya-Feldstein, J., and Ito, K. (2022). NPM1 ablation induces HSC aging and inflammation to develop myelodysplastic syndrome exacerbated by p53 loss. EMBO Rep. *23*, e54262. https://doi.org/10.15252/embr.202154262.
81. Kalamakis, G., Brüne, D., Ravichandran, S., Bolz, J., Fan, W., Ziebell, F., Stiehl, T., Catalá-Martinez, F., Kupke, J., Zhao, S., et al. (2019). Quiescence Modulates Stem Cell Maintenance and Regenerative Capacity in the Aging Brain. Cell *176*, 1407–1419.e14. https://doi.org/10.1016/j.cell.2019.01.040.
82. Harris, L., Rigo, P., Stiehl, T., Gaber, Z.B., Austin, S.H.L., Masdeu, M.D.M., Edwards, A., Urbán, N., Marciniak-Czochra, A., and Guillemot, F. (2021). Coordinated changes in cellular behavior ensure the lifelong maintenance of the hippocampal stem cell population. Cell Stem Cell *28*, 863–876.e6. https://doi.org/10.1016/j.stem.2021.01.003.
83. Wu, Y., Bottes, S., Fisch, R., Zehnder, C., Cole, J.D., Pilz, G.-A., Helmchen, F., Simons, B.D., and Jessberger, S. (2023). Chronic in vivo imaging defines age-dependent alterations of neurogenesis in the mouse hippocampus. Nat. Aging *3*, 380–390. https://doi.org/10.1038/s43587-023-00370-9.
84. Altman, J., and Das, G.D. (1965). Autoradiographic and histological evidence of postnatal hippocampal neurogenesis in rats. J. Comp. Neurol. *124*, 319–335. https://doi.org/10.1002/cne.901240303.
85. Angevine. (1965). Time of neuron origin in the hippocampal region: An autoradiographic study in the mouse. Exp. Neurol. *11*, 1–39. https://doi.org/10.1016/0014-4886(65)90121-4.
86. Seri, B., García-Verdugo, J.M., McEwen, B.S., and Alvarez-Buylla, A. (2001). Astrocytes Give Rise to New Neurons in the Adult Mammalian Hippocampus. J. Neurosci. *21*, 7153–7160. https://doi.org/10.1523/JNEUROSCI.21-18-07153.2001.
87. Gould, E., Tanapat, P., McEwen, B.S., Flügge, G., and Fuchs, E. (1998). Proliferation of granule cell precursors in the dentate gyrus of adult monkeys is diminished by stress. Proc. Natl. Acad. Sci. USA *95*, 3168–3171. https://doi.org/10.1073/pnas.95.6.3168.
88. Kornack, D.R., and Rakic, P. (1999). Continuation of neurogenesis in the hippocampus of the adult macaque monkey. Proc. Natl. Acad. Sci. USA *96*, 5768–5773. https://doi.org/10.1073/pnas.96.10.5768.

89. Ngwenya, L.B., Peters, A., and Rosene, D.L. (2006). Maturational sequence of newly generated neurons in the dentate gyrus of the young adult rhesus monkey. J. Comp. Neurol. *498*, 204–216. https://doi.org/10.1002/cne.21045.

90. Jabès, A., Lavenex, P.B., Amaral, D.G., and Lavenex, P. (2010). Quantitative analysis of postnatal neurogenesis and neuron number in the macaque monkey dentate gyrus. Eur. J. Neurosci. *31*, 273–285. https://doi.org/10.1111/j.1460-9568.2009.07061.x.

91. Kohler, S.J., Williams, N.I., Stanton, G.B., Cameron, J.L., and Greenough, W.T. (2011). Maturation time of new granule cells in the dentate gyrus of adult macaque monkeys exceeds six months. Proc. Natl. Acad. Sci. USA *108*, 10326–10331. https://doi.org/10.1073/pnas.1017099108.

92. Yuan, T.-F., Li, J., Ding, F., and Arias-Carrion, O. (2014). Evidence of adult neurogenesis in non-human primates and human. Cell Tissue Res. *358*, 17–23. https://doi.org/10.1007/s00441-014-1980-z.

93. Eriksson, P.S., Perfilieva, E., Björk-Eriksson, T., Alborn, A.-M., Nordborg, C., Peterson, D.A., and Gage, F.H. (1998). Neurogenesis in the adult human hippocampus. Nat. Med. *4*, 1313–1317. https://doi.org/10.1038/3305.

94. Knoth, R., Singec, I., Ditter, M., Pantazis, G., Capetian, P., Meyer, R.P., Horvat, V., Volk, B., and Kempermann, G. (2010). Murine Features of Neurogenesis in the Human Hippocampus across the Lifespan from 0 to 100 Years. PLoS One *5*, e8809. https://doi.org/10.1371/journal.pone.0008809.

95. Spalding, K.L., Bergmann, O., Alkass, K., Bernard, S., Salehpour, M., Huttner, H.B., Boström, E., Westerlund, I., Vial, C., Buchholz, B.A., et al. (2013). Dynamics of Hippocampal Neurogenesis in Adult Humans. Cell *153*, 1219–1227. https://doi.org/10.1016/j.cell.2013.05.002.

96. Boldrini, M., Fulmore, C.A., Tartt, A.N., Simeon, L.R., Pavlova, I., Poposka, V., Rosoklija, G.B., Stankov, A., Arango, V., Dwork, A.J., et al. (2018). Human Hippocampal Neurogenesis Persists throughout Aging. Cell Stem Cell *22*, 589–599.e5. https://doi.org/10.1016/j.stem.2018.03.015.

97. Sorrells, S.F., Paredes, M.F., Cebrian-Silla, A., Sandoval, K., Qi, D., Kelley, K.W., James, D., Mayer, S., Chang, J., Auguste, K.I., et al. (2018). Human hippocampal neurogenesis drops sharply in children to undetectable levels in adults. Nature *555*, 377–381. https://doi.org/10.1038/nature25975.

98. Moreno-Jiménez, E.P., Flor-García, M., Terreros-Roncal, J., Rábano, A., Cafini, F., Pallas-Bazarra, N., Ávila, J., and Llorens-Martín, M. (2019). Adult hippocampal neurogenesis is abundant in neurologically healthy subjects and drops sharply in patients with Alzheimer's disease. Nat. Med. *25*, 554–560. https://doi.org/10.1038/s41591-019-0375-9.

99. Tobin, M.K., Musaraca, K., Disouky, A., Shetti, A., Bheri, A., Honer, W.G., Kim, N., Dawe, R.J., Bennett, D.A., Arfanakis, K., and Lazarov, O. (2019). Human Hippocampal Neurogenesis Persists in Aged Adults and Alzheimer's Disease Patients. Cell Stem Cell *24*, 974–982.e3. https://doi.org/10.1016/j.stem.2019.05.003.

100. Franjic, D., Skarica, M., Ma, S., Arellano, J.I., Tebbenkamp, A.T.N., Choi, J., Xu, C., Li, Q., Morozov, Y.M., Andrijevic, D., et al. (2022). Transcriptomic taxonomy and neurogenic trajectories of adult human, macaque, and pig hippocampal and entorhinal cells. Neuron *110*, 452–469.e14. https://doi.org/10.1016/j.neuron.2021.10.036.

101. Zhou, Y., Su, Y., Li, S., Kennedy, B.C., Zhang, D.Y., Bond, A.M., Sun, Y., Jacob, F., Lu, L., Hu, P., et al. (2022). Molecular landscapes of human hippocampal immature neurons across lifespan. Nature *607*, 527–533. https://doi.org/10.1038/s41586-022-04912-w.

102. Bayer, S.A. (1980). Development of the hippocampal region in the rat I. Neurogenesis examined with 3H-thymidine autoradiography. J. Comp. Neurol. *190*, 87–114. https://doi.org/10.1002/cne.901900107.

103. Bayer, S.A. (1980). Development of the hippocampal region in the rat II. Morphogenesis during embryonic and early postnatal life. J. Comp. Neurol. *190*, 115–134. https://doi.org/10.1002/cne.901900108.

104. Yang, P., Zhang, J., Shi, H., Zhang, J., Xu, X., Xiao, X., and Liu, Y. (2014). Developmental profile of neurogenesis in prenatal human hippocampus: An immunohistochemical study. Int. J. Dev. Neurosci. *38*, 1–9. https://doi.org/10.1016/j.ijdevneu.2014.06.015.

105. Cipriani, S., Journiac, N., Nardelli, J., Verney, C., Delezoide, A.-L., Guimiot, F., Gressens, P., and Adle-Biassette, H. (2017). Dynamic Expression Patterns of Progenitor and Neuron Layer Markers in the Developing Human Dentate Gyrus and Fimbria. Cerebr. Cortex *27*, 358–372. https://doi.org/10.1093/cercor/bhv223.

106. Cipriani, S., Ferrer, I., Aronica, E., Kovacs, G.G., Verney, C., Nardelli, J., Khung, S., Delezoide, A.-L., Milenkovic, I., Rasika, S., et al. (2018). Hippocampal Radial Glial Subtypes and Their Neurogenic Potential in Human Fetuses and Healthy and Alzheimer's Disease Adults. Cerebr. Cortex *28*, 2458–2478. https://doi.org/10.1093/cercor/bhy096.

107. Bond, A.M., Berg, D.A., Lee, S., Garcia-Epelboim, A.S., Adusumilli, V.S., Ming, G.L., and Song, H. (2020). Differential Timing and Coordination of Neurogenesis and Astrogenesis in Developing Mouse Hippocampal Subregions. Brain Sci. *10*, 909. https://doi.org/10.3390/brainsci10120909.

108. Bond, A.M., Ming, G.L., and Song, H. (2022). What Is the Relationship Between Hippocampal Neurogenesis Across Different Stages of the Lifespan? Front. Neurosci. *16*, 891713.

109. Amrein, I., Isler, K., and Lipp, H.-P. (2011). Comparing adult hippocampal neurogenesis in mammalian species and orders: influence of chronological age and life history stage. Eur. J. Neurosci. *34*, 978–987. https://doi.org/10.1111/j.1460-9568.2011.07804.x.

110. Charvet, C.J., and Finlay, B.L. (2018). Comparing Adult Hippocampal Neurogenesis Across Species: Translating Time to Predict the Tempo in Humans. Front. Neurosci. *12*, 706.

111. Snyder, J.S. (2019). Recalibrating the Relevance of Adult Neurogenesis. Trends Neurosci. *42*, 164–178. https://doi.org/10.1016/j.tins.2018.12.001.

112. Gao, X., Xu, C., Asada, N., and Frenette, P.S. (2018). The hematopoietic stem cell niche: from embryo to adult. Development *145*, dev139691. https://doi.org/10.1242/dev.139691.

113. Gros, J., Manceau, M., Thomé, V., and Marcelle, C. (2005). A common somitic origin for embryonic muscle progenitors and satellite cells. Nature *435*, 954–958. https://doi.org/10.1038/nature03572.

114. Relaix, F., Rocancourt, D., Mansouri, A., and Buckingham, M. (2005). A Pax3/Pax7-dependent population of skeletal muscle progenitor cells. Nature *435*, 948–953. https://doi.org/10.1038/nature03594.

115. Kassar-Duchossoy, L., Giacone, E., Gayraud-Morel, B., Jory, A., Gomès, D., and Tajbakhsh, S. (2005). Pax3/Pax7 mark a novel population of primitive myogenic cells during development. Genes Dev. *19*, 1426–1431. https://doi.org/10.1101/gad.345505.

116. Guiu, J., Hannezo, E., Yui, S., Demharter, S., Ulyanchenko, S., Maimets, M., Jørgensen, A., Perlman, S., Lundvall, L., Mamsen, L.S., et al. (2019). Tracing the origin of adult intestinal stem cells. Nature *570*, 107–111. https://doi.org/10.1038/s41586-019-1212-5.

117. Redmond, S.A., Figueres-Oñate, M., Obernier, K., Nascimento, M.A., Parraguez, J.I., López-Mascaraque, L., Fuentealba, L.C., and Alvarez-Buylla, A. (2019). Development of Ependymal and Postnatal Neural Stem Cells and Their Origin from a Common Embryonic Progenitor. Cell Rep. *27*, 429–441.e3. https://doi.org/10.1016/j.celrep.2019.01.088.

118. Picard, C.A., and Marcelle, C. (2013). Two distinct muscle progenitor populations coexist throughout amniote development. Dev. Biol. *373*, 141–148. https://doi.org/10.1016/j.ydbio.2012.10.018.

119. Christensen, J.L., Wright, D.E., Wagers, A.J., and Weissman, I.L. (2004). Circulation and Chemotaxis of Fetal Hematopoietic Stem Cells. PLoS Biol. *2*, e75. https://doi.org/10.1371/journal.pbio.0020075.

120. Hall, T.D., Kim, H., Dabbah, M., Myers, J.A., Crawford, J.C., Morales-Hernandez, A., Caprio, C.E., Sriram, P., Kooienga, E., Derecka, M., et al. (2022). Murine fetal bone marrow does not support functional

hematopoietic stem and progenitor cells until birth. Nat. Commun. *13*, 5403. https://doi.org/10.1038/s41467-022-33092-4.

121. Bowie, M.B., McKnight, K.D., Kent, D.G., McCaffrey, L., Hoodless, P.A., and Eaves, C.J. (2006). Hematopoietic stem cells proliferate until after birth and show a reversible phase-specific engraftment defect. J. Clin. Invest. *116*, 2808–2816. https://doi.org/10.1172/JCI28310.
122. Baser, A., Skabkin, M., Kleber, S., Dang, Y., Gülcüler Balta, G.S., Kalamakis, G., Göpferich, M., Ibañez, D.C., Schefzik, R., Lopez, A.S., et al. (2019). Onset of differentiation is post-transcriptionally controlled in adult neural stem cells. Nature *566*, 100–104. https://doi.org/10.1038/s41586-019-0888-x.
123. Wang, R., and Amoyel, M. (2022). mRNA Translation Is Dynamically Regulated to Instruct Stem Cell Fate. Front. Mol. Biosci. *9*, 863885. https://doi.org/10.3389/fmolb.2022.863885.
124. Blanco, S., Bandiera, R., Popis, M., Hussain, S., Lombard, P., Aleksic, J., Sajini, A., Tanna, H., Cortés-Garrido, R., Gkatza, N., et al. (2016). Stem cell function and stress response are controlled by protein synthesis. Nature *534*, 335–340. https://doi.org/10.1038/nature18282.
125. Signer, R.A.J., Magee, J.A., Salic, A., and Morrison, S.J. (2014). Haematopoietic stem cells require a highly regulated protein synthesis rate. Nature *509*, 49–54. https://doi.org/10.1038/nature13035.
126. Machado, L., Esteves de Lima, J., Fabre, O., Proux, C., Legendre, R., Szegedi, A., Varet, H., Ingerslev, L.R., Barrès, R., Relaix, F., and Mourikis, P. (2017). In Situ Fixation Redefines Quiescence and Early Activation of Skeletal Muscle Stem Cells. Cell Rep. *21*, 1982–1993. https://doi.org/10.1016/j.celrep.2017.10.080.
127. Boonsanay, V., Zhang, T., Georgieva, A., Kostin, S., Qi, H., Yuan, X., Zhou, Y., and Braun, T. (2016). Regulation of Skeletal Muscle Stem Cell Quiescence by Suv4-20h1-Dependent Facultative Heterochromatin Formation. Cell Stem Cell *18*, 229–242. https://doi.org/10.1016/j.stem.2015.11.002.
128. Cebrián-Silla, A., Alfaro-Cervelló, C., Herranz-Pérez, V., Kaneko, N., Park, D.H., Sawamoto, K., Alvarez-Buylla, A., Lim, D.A., and García-Verdugo, J.M. (2017). Unique Organization of the Nuclear Envelope in the Post-natal Quiescent Neural Stem Cells. Stem Cell Rep. *9*, 203–216. https://doi.org/10.1016/j.stemcr.2017.05.024.
129. Takubo, K., Nagamatsu, G., Kobayashi, C.I., Nakamura-Ishizu, A., Kobayashi, H., Ikeda, E., Goda, N., Rahimi, Y., Johnson, R.S., Soga, T., et al. (2013). Regulation of glycolysis by Pdk functions as a metabolic checkpoint for cell cycle quiescence in hematopoietic stem cells. Cell Stem Cell *12*, 49–61. https://doi.org/10.1016/j.stem.2012.10.011.
130. Wang, Y.-H., Israelsen, W.J., Lee, D., Yu, V.W.C., Jeanson, N.T., Clish, C.B., Cantley, L.C., Vander Heiden, M.G., and Scadden, D.T. (2014). Cell-state-specific metabolic dependency in hematopoiesis and leukemogenesis. Cell *158*, 1309–1323. https://doi.org/10.1016/j.cell.2014.07.048.
131. Flores, A., Schell, J., Krall, A.S., Jelinek, D., Miranda, M., Grigorian, M., Braas, D., White, A.C., Zhou, J.L., Graham, N.A., et al. (2017). Lactate dehydrogenase activity drives hair follicle stem cell activation. Nat. Cell Biol. *19*, 1017–1026. https://doi.org/10.1038/ncb3575.
132. Beckervordersandforth, R., Ebert, B., Schäffner, I., Moss, J., Fiebig, C., Shin, J., Moore, D.L., Ghosh, L., Trinchero, M.F., Stockburger, C., et al. (2017). Role of Mitochondrial Metabolism in the Control of Early Lineage Progression and Aging Phenotypes in Adult Hippocampal Neurogenesis. Neuron *93*, 560–573.e6. https://doi.org/10.1016/j.neuron.2016.12.017.
133. Simsek, T., Kocabas, F., Zheng, J., DeBerardinis, R.J., Mahmoud, A.I., Olson, E.N., Schneider, J.W., Zhang, C.C., and Sadek, H.A. (2010). The Distinct Metabolic Profile of Hematopoietic Stem Cells Reflects Their Location in a Hypoxic Niche. Cell Stem Cell *7*, 380–390. https://doi.org/10.1016/j.stem.2010.07.011.
134. Liang, R., Arif, T., Kalmykova, S., Kasianov, A., Lin, M., Menon, V., Qiu, J., Bernitz, J.M., Moore, K., Lin, F., et al. (2020). Restraining Lysosomal Activity Preserves Hematopoietic Stem Cell Quiescence and Potency. Cell Stem Cell *26*, 359–376.e7. https://doi.org/10.1016/j.stem.2020.01.013.
135. Li, B., and Dewey, C.N. (2011). RSEM: accurate transcript quantification from RNA-Seq data with or without a reference genome. BMC Bioinf. *12*, 323. https://doi.org/10.1186/1471-2105-12-323.
136. Martin, M. (2011). Cutadapt removes adapter sequences from high-throughput sequencing reads. EMBnet. j. *17*, 10–12. https://doi.org/10.14806/ej.17.1.200.
137. Li, H., Handsaker, B., Wysoker, A., Fennell, T., Ruan, J., Homer, N., Marth, G., Abecasis, G., Durbin, R., and Subgroup, 1000 Genome Project Data Processing (2009). The Sequence Alignment/Map format and SAMtools. Bioinformatics *25*, 2078. https://doi.org/10.1093/bioinformatics/btp352.
138. Qiu, X., Mao, Q., Tang, Y., Wang, L., Chawla, R., Pliner, H.A., and Trapnell, C. (2017). Reversed graph embedding resolves complex single-cell trajectories. Nat. Methods *14*, 979–982. https://doi.org/10.1038/nmeth.4402.
139. Zappia, L., and Oshlack, A. (2018). Clustering trees: a visualization for evaluating clusterings at multiple resolutions. GigaScience *7*, giy083. https://doi.org/10.1093/gigascience/giy083.
140. Hafemeister, C., and Satija, R. (2019). Normalization and variance stabilization of single-cell RNA-seq data using regularized negative binomial regression. Genome Biology *20*, 296. https://doi.org/10.1186/s13059-019-1874-1.
141. Hao, Y., Hao, S., Andersen-Nissen, E., Mauck, W.M., Zheng, S., Butler, A., Lee, M.J., Wilk, A.J., Darby, C., Zager, M., et al. (2021). Integrated analysis of multimodal single-cell data. Cell *184*, 3573–3587.e29. https://doi.org/10.1016/j.cell.2021.04.048.
142. Soneson, C., Matthes, K.L., Nowicka, M., Law, C.W., and Robinson, M.D. (2016). Isoform prefiltering improves performance of count-based methods for analysis of differential transcript usage. Genome Biol. *17*, 12. https://doi.org/10.1186/s13059-015-0862-3.
143. Lun, A., and Hicks, S. (2022). Bluster: Clustering Algorithm for Bioconductor.
144. Yu, G., Wang, L.-G., Han, Y., and He, Q.-Y. (2012). clusterProfiler: an R Package for Comparing Biological Themes Among Gene Clusters. OMICS *16*, 284–287. https://doi.org/10.1089/omi.2011.0118.
145. Dobin, A., Davis, C.A., Schlesinger, F., Drenkow, J., Zaleski, C., Jha, S., Batut, P., Chaisson, M., and Gingeras, T.R. (2013). STAR: ultrafast universal RNA-seq aligner. Bioinformatics *29*, 15–21. https://doi.org/10.1093/bioinformatics/bts635.
146. Aibar, S., González-Blas, C.B., Moerman, T., Huynh-Thu, V.A., Imrichova, H., Hulselmans, G., Rambow, F., Marine, J.-C., Geurts, P., Aerts, J., et al. (2017). SCENIC: single-cell regulatory network inference and clustering. Nat. Methods *14*, 1083–1086. https://doi.org/10.1038/nmeth.4463.
147. Lun, A.T.L., McCarthy, D.J., and Marioni, J.C. (2016). A step-by-step workflow for low-level analysis of single-cell RNA-seq data with Bioconductor. F1000Res. *5*, 2122. https://doi.org/10.12688/f1000research.9501.2.
148. McCarthy, D.J., Campbell, K.R., Lun, A.T.L., and Wills, Q.F. (2017). Scater: pre-processing, quality control, normalization and visualization of single-cell RNA-seq data in R. Bioinformatics *33*, 1179–1186. https://doi.org/10.1093/bioinformatics/btw777.
149. Takeda, N., Jain, R., LeBoeuf, M.R., Wang, Q., Lu, M.M., and Epstein, J.A. (2011). Interconversion Between Intestinal Stem Cell Populations in Distinct Niches. Science *334*, 1420–1424. https://doi.org/10.1126/science.1213214.
150. Muzumdar, M.D., Tasic, B., Miyamichi, K., Li, L., and Luo, L. (2007). A global double-fluorescent Cre reporter mouse. genesis *45*, 593–605. https://doi.org/10.1002/dvg.20335.
151. Ramsköld, D., Luo, S., Wang, Y.-C., Li, R., Deng, Q., Faridani, O.R., Daniels, G.A., Khrebtukova, I., Loring, J.F., Laurent, L.C., et al. (2012). Full-length mRNA-Seq from single-cell levels of RNA and individual circulating tumor cells. Nat. Biotechnol. *30*, 777–782. https://doi.org/10.1038/nbt.2282.

152. Picelli, S., Björklund, Å.K., Faridani, O.R., Sagasser, S., Winberg, G., and Sandberg, R. (2013). Smart-seq2 for sensitive full-length transcriptome profiling in single cells. Nat. Methods *10*, 1096–1098. https://doi.org/10.1038/nmeth.2639.

153. Hao, Y., Hao, S., Andersen-Nissen, E., Mauck, W.M., Zheng, S., Butler, A., Lee, M.J., Wilk, A.J., Darby, C., Zager, M., et al. (2021). Integrated analysis of multimodal single-cell data. Cell *184*, 3573–3587.e29. https://doi.org/10.1016/j.cell.2021.04.048.

154. Kaufman, L., and Rousseeuw, P.J. (1990). Finding Groups in Data: An Introduction to Cluster Analysis.

155. Stuart, T., Butler, A., Hoffman, P., Hafemeister, C., Papalexi, E., Mauck, W.M., Hao, Y., Stoeckius, M., Smibert, P., and Satija, R. (2019). Comprehensive Integration of Single-Cell Data. Cell *177*, 1888–1902.e21. https://doi.org/10.1016/j.cell.2019.05.031.

156. Huynh-Thu, V.A., Irrthum, A., Wehenkel, L., and Geurts, P. (2010). Inferring Regulatory Networks from Expression Data Using Tree-Based Methods. PLoS One *5*, e12776. https://doi.org/10.1371/journal.pone.0012776.

157. Cahan, P., Li, H., Morris, S.A., Lummertz da Rocha, E., Daley, G.Q., and Collins, J.J. (2014). CellNet: network biology applied to stem cell engineering. Cell *158*, 903–915. https://doi.org/10.1016/j.cell.2014.07.020.

158. Faith, J.J., Hayete, B., Thaden, J.T., Mogno, I., Wierzbowski, J., Cottarel, G., Kasif, S., Collins, J.J., and Gardner, T.S. (2007). Large-Scale Mapping and Validation of Escherichia coli Transcriptional Regulation from a Compendium of Expression Profiles. PLoS Biol. *5*, e8. https://doi.org/10.1371/journal.pbio.0050008.

159. Wu, T., Hu, E., Xu, S., Chen, M., Guo, P., Dai, Z., Feng, T., Zhou, L., Tang, W., Zhan, L., et al. (2021). clusterProfiler 4.0: A universal enrichment tool for interpreting omics data. Innovation *2*, 100141. https://doi.org/10.1016/j.xinn.2021.100141.

160. Yuan, R., Hahn, Y., Stempel, M.H., Sidibe, D.K., Laxton, O., Chen, J., Kulkarni, A., and Maday, S. (2023). Proteasomal inhibition preferentially stimulates lysosome activity relative to autophagic flux in primary astrocytes. Autophagy *19*, 570–596. https://doi.org/10.1080/15548627.2022.2084884.

STAR★METHODS

KEY RESOURCES TABLE

REAGENT or RESOURCE	SOURCE	IDENTIFIER
Antibodies		
Mouse anti-Flag	Sigma-Aldrich	Cat# F1804; RRID: AB_262044
Goat anti-Mcm2	R&D Systems	Cat# AF5778; RRID: AB_2141963
Rabbit anti-Geminin	Proteintech	Cat# 10802-1-AP; RRID: AB_2110945
Rabbit anti-phospho-histone H3 (SER10)	Cell Signaling Technology	Cat# 53348S; RRID: AB_2799431
Rabbit anti-Sox9	Millipore	Cat# AB5535; RRID: AB_2239761
Rabbit anti-Nfix	Thermo Fisher Scientific	Cat# PA5-30897; RRID: AB_2548371
Goat anti-GFP	Rockland Inc.	Cat#600-101-215 RRID: AB_218182
Mouse anti-Mcm2 (BM28)	BD Biosciences	Cat#610701 RRID: AB_398024
Rabbit anti-Hopx	Proteintech	Cat# 11419-1-AP; RRID: AB_10693525
Rabbit anti-Prox1	Abcam	Cat# ab199359; RRID: AB_2868427
Chemicals, peptides, and recombinant proteins		
DAPI	Roche	10236276001
DAPI	BD Biosciences	564907
Paraformaldehyde	Electron Microscopy Sciences	100504–162
Triton X-100	Sigma-Aldrich	T9284
Donkey serum	Millipore-Sigma	S30-100ML
TFM Tissue Freezing Medium	GeneralData	TFM-5
ProLong™ Gold Antifade Mountant	Thermo Fisher Scientific	P36930
Percoll	GE Healthcare	17-0891-02
Hibernate A	Brain Bits	HA
Hibernate A Low Fluorescence	Brain Bits	HALF
Hibernate E Low Fluorescence	Brain Bits	HELF
MitoTracker™ Deep Red FM - Special Packaging	Thermo Fisher Scientific	M22426
Dihydroethidium	Thermo Fisher Scientific	D1168
Autophagy Assay Kit (Red)	Abcam	ab270790
Target Retrieval Solution, Concentrated x 10	Agilent Dako	S169984-2
Chloroquine diphosphate salt	Sigma-Aldrich	C6628-25G
Bafilomycin A1	Sigma-Aldrich	19–148
OPP (O-propargyl-puromycin)	Click Chemistry Tools	1407–5
DMEM	Gibco	11965084
Fetal Bovine Serum	Hyclone	SH30071.03
Glutamax	Gibco	35050061
Penicillin-Streptomycin	Gibco	15140122
Poly-L-lysine	Sigma-Aldrich	P2636
B-27	Gibco	17504044
Critical commercial assays		
MACS Neural Tissue Dissociation Kit (P)	Miltenyi Biotec	130-092-628
Click-iT™ Plus OPP Alexa Fluor™ 647 Protein Synthesis Assay Kit	Thermo Fisher Scientific	C10458
Agencourt RNAClean XP	Beckman Coulter	A63987
SMARTScribe Reverse Transcriptase	Clontech	639538
Advantage 2 PCR Kit	Clontech	639206
KAPA HiFi PCR Kit with dNTPs	KAPA	KK2102
Qubit dsDNA HS Assay Kit	Thermo Fisher Scientific	Q32854

(*Continued on next page*)

Continued

REAGENT or RESOURCE	SOURCE	IDENTIFIER
EZ-Tn5 Custom Transposome Construction Kit with pMOD-2 Transposon Construction Vector	Epicenter	TNP10622
75-cycle High Output Kit v2.5	Illumina	20024906
Click-iT™ Plus EdU Alexa Fluor™ 647 Flow Cytometry Assay Kit	Thermo Fisher Scientific	C10634
Deposited data		
scRNA-seq data	This Paper	NCBI GEO: GSE232833
Experimental models: Organisms/strains		
Mouse: Hopx$^{tm3.1Joe}$/J	The Jackson Laboratory	Cat# 029271; RRID: IMSR_JAX:029271
Mouse: GFP-LC3	RIKEN BioResource Research Center	Cat# RBRC00806; RRID: IMSR_RBRC00806
Mouse: C57BL/6NCrl	Charles River Laboratory	Cat# CRL:27; RRID: IMSR_CRL:27
Mouse: *Hopx$^{tm2.1(cre/ERT2)Joe}$*/J	The Jackson Laboratory	Cat# 017606; RRID: IMSR_JAX:017606
Mouse: B6.129(Cg)-Gt(ROSA) 26Sor$^{tm4(ACTB-tdTomato,-EGFP)Luo}$/J	The Jackson Laboratory	Cat# 007676; RRID: IMSR_JAX:007676
Mouse: B6.129S-Atg5<tm1Myok>	RIKEN BioResource Research Center	Cat# RBRC02975; RRID: IMSR_RBRC02975
Oligonucleotides		
SMARTSeq_CDS_Primer	AACGAGTGGAATCACTG CTGAGTACTTTTTTTTTTT TTTTTTTTTTTTTTTTTTVN	
SMARTSeq_Amp	AACGAGTGGAATCACTGCTGAGT	
SMARTSeq_TSO_RNAOligo	AACGAGTGGAATCACTGCTG AGTACATrGrG+G	
Software and algorithms		
Code	This Paper	GitHub: https://github.com/dvjim/AtoQ
ImageJ	NIH	https://imagej.nih.gov/ij/
GraphPad Prism	GraphPad Software Inc	https://www.graphpad.com/scientific-software/prism/
FlowJo	FlowJO, LLC	https://www.flowjo.com/
BD FACSDiva™	BD Biosciences	https://www.bdbiosciences.com/en-us/products/software/instrument-software/bd-facsdiva-software
R	Open source	https://www.r-project.org/
RSEM	Li and Dewey[135]	https://deweylab.github.io/RSEM/
Cutadapt	Martin[136]	https://cutadapt.readthedocs.io/en/stable/
Samtools	Li et al., 2009[137]	http://www.htslib.org/
Monocle	Qiu et al.[138]	http://cole-trapnell-lab.github.io/monocle-release/
Clustree	Zappia and Oshlack[139]	http://lazappi.github.io/clustree.
Seurat	Satija and Hafemeister, 2019[140]; Hao et al., 2020[141]	https://satijalab.org/seurat/
Tximport	Soneson et al.[142]	https://github.com/mikelove/tximport
CellRouter	Lummertz da Rocha et al.[57]	https://github.com/edroaldo/cellrouter
bluster	Lun and Hicks[143]	https://bioconductor.org/packages/release/bioc/html/bluster.html
ClusterProfiler	Yu et al.[144]	https://yulab-smu.top/software/
VelocytoR	La Manno et al.[46]	http://velocyto.org/
STAR	Dobin et al.[145]	https://github.com/alexdobin/STAR/releases

(*Continued on next page*)

Continued

REAGENT or RESOURCE	SOURCE	IDENTIFIER
SCENIC	Aibar et al.[146]	https://scenic.aertslab.org/
Adobe Illustrator	Adobe	https://www.adobe.com/products/illustrator.html; RRID: SCR_010279
Adobe Photoshop	Adobe	https://www.adobe.com/products/photoshop.html; RRID:SCR_014199
Zen 2	Carl Zeiss	https://www.zeiss.com; RRID: SCR_013672
scuttle	Lun et al.[147]; McCarthy et al.[148]	https://bioconductor.org/packages/release/bioc/html/scuttle.html
Other		
Fluorodish	World Precision Instruments	FD35-100

RESOURCE AVAILABILITY

Lead contact

Further information and requests for resources and reagents should be directed to and will be fulfilled by the Lead Contact, Hongjun Song (shongjun@pennmedicine.upenn.edu)

Materials availability

This study did not generate new unique reagents.

Data and code availability

Single-cell RNA-seq data have been deposited at the NCBI GEO: GSE232833. All original code has been deposited at GitHub: https://github.com/dvjim/AtoQ. Microscopy data reported in this paper will be shared by the lead contact upon request. Any additional information required to reanalyze the data reported in this paper is available from the lead contact upon request.

EXPERIMENTAL MODEL AND STUDY PARTICIPANT DETAILS

Animals

All animal procedures used in this study were performed in accordance with protocols approved by the Institutional Animal Care and Use Committee of the University of Pennsylvania. Animals were housed in a 14 h light/10 h dark cycle with food and water *ad libitum*. Both male and female mice from the same litters were used for all experiments and data were pooled together. *Hopx*^{3FlagGFP} knock-in mice (Jackson #029271; RRID #IMSR_JAX:029271) harboring a 3xFLAG tagged HOPX and EGFP under the *Hopx* promoter were used to visualize *Hopx* expression in the brain and to identify and isolate *Hopx*-expressing cells from the DG.[39] *Hopx*^{3FlagGFP} transgenic mice used in this study were back-crossed for at least five generations and maintained on a C57BL/6 background. *Hopx*$^{3FlagGFP/+}$ genotyped mice were used in all experiments. GFP-LC3 mice (RIKEN BioResource Research Center #RBRC00806; strain name B6.Cg-Tg(CAG-EGFP/LC3)53Nmi/NmiRbrc; GFP-LC3#53; RRID # IMSR_RBRC00806) expressing a fusion cDNA encoding enhanced GFP jointed at its C terminus to rat microtubule-associated protein 1 light chain 3 beta under the control of the CAG promoter were used to visualize the occurrence of autophagy.[65] The GFP-LC3 transgenic mouse line was maintained as heterozygotes bred to C57BL/6. Triple transgenic *Hopx-CreER*^{T2}*::mTmG; Atg5*$^{Flx/Flx}$ mice were generated by mating the following three transgenic mouse lines: (1) *Hopx-CreER*^{T2} knock-in mice (Jackson #017606; RRID # IMSR_JAX:017606) that harbor a tamoxifen-inducible *CreER*^{T2} fusion gene,[149] (2) *Rosa26*$^{flox\text{-}mT\text{-}stop\text{-}flox\text{-}mG}$ mice (Jackson #007676; RRID # IMSR_JAX:007676), which harbor *loxP* sites on either side of a membrane-targeted tdTomato (mT) cassette followed by an STOP sequence, upstream of a membrane-target EGFP (mG) cassette, such that in the presence of Cre the mT cassette is deleted, replaced by mG expression,[150] and (3) *Atg5*$^{Flx/Flx}$ mice (RIKEN BioResource Research Center # RBRC02975; strain name B6.129S-Atg5<tm1Myok>; RRID # IMSR_RBRC02975), in which Exon 3 of the *Atg5* gene is flanked by *loxP* sites.[76] *Hopx-CreER*^{T2}*::mTmG; Atg5*$^{w/w}$ and *Hopx-CreER*^{T2}*::mTmG; Atg5*$^{Flx/Flx}$ mice were generated as littermates and used for experimentation. Transgenic mice were genotyped using primer sets provided by The Jackson Laboratory or RIKEN BioResource Research Center. Genomic DNA was isolated in a solution of 25 mM NaOH and 0.2 mM EDTA at 95°C for 1 h, followed by vortexing and centrifugation.

METHOD DETAILS

Tissue processing and immunohistology

Animals were transcardially perfused with ice-cold DPBS, followed by ice-cold 4% paraformaldehyde (PFA). Brains were fixed for 2 h in 4% PFA at 4°C, and then cryoprotected in 30% sucrose solution in 1x PBS overnight at 4°C. Brains were frozen in Tissue Freezing

Medium (GeneralData) and stored at −80°C until coronal brain sections (25 μm) were collected onto Fisherbrand Superfrost Plus Microscope Slides (Fisher Scientific, 12-550-15) using a cryostat (Leica, CM3050S). Slides with brain sections were stored at −20°C until immunohistochemistry was performed.

All immunostaining was performed in sets that included sections from each age being analyzed to prevent the potentially confounding batch effects of doing multiple sets of immunostaining. Antibodies used in this study can be found in the key resources table. Mouse anti-Flag (Sigma, Cat# F1804) was used to identify *Hopx*$^{3FlagGFP+}$ cells, denoted in images simply as "HOPX". Slides with brain sections were washed in TBS with 0.05% Triton X-100 and then underwent antigen retrieval: sections were incubated in 1x Target Retrieval Solution (Agilent Dako) at ∼95°C in a steamer for 30 min and cooled to room temperature for 45 min. Slides were then washed in TBS with 0.05% Triton X-100 and incubated in primary antibody solution (3.33% donkey serum and 0.05% Triton X-100 in TBS) overnight at 4°C. Slides were washed in PBS and then incubated in secondary antibody solution (3.33% donkey serum and 0.05% Triton X-100 in TBS) and DAPI nuclear stain (Roche) for 1–2 h at room temperature. Alexa Fluor 488, 555, 647 (Invitrogen) secondary antibodies were used at 1:250 dilutions and DAPI was used at a 1:1000 dilution. After a second set of PBS washes, sections were mounted with ProLong Gold Antifade Mountant (Thermo Fisher Scientific). If GFP immunostaining was performed in conjunction with other antibodies, then GFP primary and secondary antibody steps were completed prior to antigen retrieval. All brain sections from *Hopx-CreER*^{T2}*::mTmG* mice underwent antigen retrieval to quench the endogenous mTomato signal.

Confocal microscopy and image processing

Brain sections were imaged using a Zeiss LSM 810 confocal microscope (Carl Zeiss). Either 40X or 63X objectives were used for imaging. For each imaging experiment, the exact same imaging settings (laser power and gain) were used to image sections from each staining set to reduce variability. Images were analyzed using ImageJ software.

Single-cell RNA-sequencing

Dentate gyrus dissection and dissociation

DG was rapidly dissected from fresh *Hopx*$^{3FlagGFP/+}$ mouse brain in ice-cold DPBS under a dissecting microscope. Tissue was then dissociated using a MACS Neural Tissue Dissociation Kit with Papain (Miltenyi Biotec, 130-092-628) according to the manufacturer's guidelines. The single cell suspension was then resuspended in 22% Percoll in Hibernate A (Brain Bits) and spun for 10 min at 700 g at 4°C without brakes. The myelin/debris supernatant was removed and the cell pellet was resuspended in Hibernate A Low Fluorescence (Brain Bits). Cells were incubated with a 1:50,000 dilution of MitoTracker Deep Red FM (Thermo Fisher Scientific) for 2 min at room temperature to label viable cells, and then were washed and put through a cell-strainer. GFP$^{+/-}$ cells were sorted using a BD FACS Aria II SORP cell sorter. Cells were collected at P3 (8 pups pooled), P7 (8 pups pooled), or P14 (8 pups pooled) and sorted into individual wells of a 96-well plate containing 2.85 μL SMART-Seq lysis buffer.

Sequencing library preparation

Library preparation was performed as previously described with minor adjustments for pg concentrations.[16] Briefly, mRNA was isolated from single cells using the SMART-seq protocol[151] and incubated at 72°C for 3 min in lysis buffer. A custom-designed primer with a 30-deoxythymidine anchor (1 μL of 12 μM) was added and incubated at 72°C for 3 min to anneal the poly-adenylated RNA. First-strand synthesis was performed using a custom-designed TSO oligo by adding 6.05 μL of RT buffer (1 μL SMARTScribe Transcriptase RT, 0.3 μL 200 mM $MgCl_2$, 0.5 μL RNase inhibitor, 1 μL dNTP, 0.25 μL 100 mM DTT, 1 μL of 12 μM TSO) to the lysed cell sample. Cells were incubated at 42°C for 90 min, followed by enzyme inactivation at 70°C for 10 min. RT product was amplified for 20 cycles using the Advantage 2 Polymerase system (2 μL of Advantage 2 Polymerase, 2 μL of dNTPs, 2 μL 12 μM custom-designed amplifying PCR primer, 29 μL of water) and PCR thermocycling with following parameters: 95°C 1 min, 95°C 15 s, 65°C 30 s, 68°C 6 min, 72°C 10 min with a final extension at 72°C 10 min. PCR products were purified using a 1:1 ratio of SPRI Beads and cDNA concentration was measured by Qubit.

Tagmentation was performed using a homemade Tn5 enzyme-buffer system, which included a Tn5 enzyme at 1:32 dilution and 2XTD buffer (20 mM TAPS-NaOH, 10 mM $MgCl_2$ and 8%PEG-8000).[43,152] Each 5 μL tagmentation reaction was incubated at 55°C for 10 min and immediately quenched using 1.25 μL 0.2% SDS. After quenching, Universal Illumina barcodes and 2x KAPA HiFi HotStart ReadyMix were used to amplify the library, bringing the reaction to 50 μL. PCR thermocycling with the following parameters was used: 72°C 5 min, 95°C 1 min, 95°C 20 s, 55°C 30 s, 72°C 30 s with a final extension at 72°C 1 min for X15 cycles. PCR products were purified using a 1:1 ratio of SPRI Beads and cDNA concentration was measured by Qubit.

Sequencing, reads alignment and pre-processing

Samples were then multiplexed at equal nM concentration to the lowest library concentration, and all libraries from each age were pooled 1:1, then diluted to a final concentration of 2 nM and sequenced on an Illumina NextSeq 550 instrument using Illumina 75-cycle High Output Kit v2.5 (20024906). The raw data was converted to ".fastq" files using bcl2fastq (v2.17.1) software. Single-end sequencing reads were pre-processed trimmed of sequencing adaptors and poly-A sequence contaminants using Cutadapt.[136] To digitally count at gene-level, the RSEM (v.1.2.28) package[135] where fastq files were imported, which outputs STAR (v.2.7.1a)[145] summarized estimates of gene-level counts using mouse reference genome assembly (GRCm38 Mouse Gencode release V19). Tximport package (v. 1.18.0)[142] was then used to concatenate individualized cell output as a matrix using gene-level RSEM settings. Raw digital expression matrices were generated, and we observed a range of gene expressions in different samples due to variability of sequencing depth.

Quality control, cell clustering and visualization

A raw expression matrix for cells was loaded as log transformed TPM value Seurat objects (v 4.0.2)[153] in R (v4.0.3) using the function ''CreateSeuratObject''. Summed gene expression count across all cells <200 TPM were discarded, cells with <500 or >7000 genes expressed were discarded, cells with >10% genes mapped to mitochondrial genes were discarded, and the retained cells underwent library size normalization with scuttle (v1.0.4) and SCT transformation with Seurat.[147,148,153] Due to the nature of our samples, we did not regress out cycling genes for downstream analysis. To cluster cells, we performed density peak clustering from Monocle (v.2.18.0)[138] using the 'clusterCells' function with 'dpFeautres' default settings. To visualize cells we used principal component analysis (PCA) and uniform manifold approximation and projection (UMAP) with the 'RunPCA' and 'RunUMAP' functions in Seurat. Three methods were used to determine the optimal range of clusters and number of principal components for downstream analysis: (1) the WSS and 'elbow'; (2) the 'Silhouette' method using 'approxSilhouette' from bluster (v1.0.0)[143,154]; and (3) hierarchical clustering from clustree (v0.5.0).[139] The elbow method assessed the total intra-cluster variation by way of within-cluster-sum of squared error as a function of the number of clusters and assessed the percentage of variance explained by successive PCs to select the optimal PC to linearize cell-cell relationships.[34] The Silhouette method uses the silhouette coefficients of over a range of k clusters, 2–8, to measure the consistency of similarity of each cell in one cluster to cells in the neighboring clusters and identify the peak as the optimum, k.[154] Clustree allows for visual interrogation of over clustering as cluster resolution increases.[139] Final evaluation of cluster separation by graph-based clusters was done using pairwise modularity between communities, which observed the total weights of edges between nodes of the same cluster using 'pairwiseModularity' function, and cluster purity quantifying the degree to which cells from multiple clusters intermingled in expression space via the 'neighborPurity' function from bluster. The resulting cell clusters were projected to the UMAP previously computed for visualizations, while PCA cell embeddings were used for RNA velocity analysis. The stability of cluster identity across P3, P7, and P14 was assessed using Pearson's correlation via pseudo-bulk analysis, which showed high correlation of cluster signatures across age samples. To remove ependymal cell contamination, we selected out cells with expression of *Foxj1*. Mature astrocytes were identified in this dataset by using Monocle's 'newCellTypeHierarchy' function and gene expression of *Abhd3* > 3, *Gjb6* $\geq$ 1, and *Gabrg1* >0. These genes were used to distinguish astrocytes from NSCs because they have previously been identified to be highly expressed in mature astrocytes and lowly expressed in adult DG NSCs.[27,34] To benchmark our assigned cell type identities, we conducted a comprehensive analysis that involved a Pearson's correlation test of our astroglial lineage clusters (ImA and MA). These clusters were compared with astroglial lineage and NSC clusters (Astro-adult, Astro-juv, Immature-Astro, RGL, RGL_young) obtained from the Hochgerner et al. dataset,[27] a single-cell RNA-seq dataset of the developing mouse hippocampus. In addition to this developmental dataset, we performed a comparative analysis by juxtaposing our data with an adult DG cell dataset.[34] This comparison aimed to evaluate and validate the activity and quiescence of our cells, while also anticipating the future (adult) distribution of q2 and MA clusters. To achieve these objectives, we integrated normalized matrices, using the Hochgerner et al.[31] clustering as an anchoring criterion through Seurat's canonical correlation analysis based integration workflow ('FindIntegrationAnchors' and 'IntegrateData' functions).[155] The resulting manifold, featuring 7 clusters, was employed for downstream analysis. Subsequently, we directly compared this validated manifold with the Shin et al. dataset[40] using the same integration methods, ensuring a consistent and reliable comparative assessment across each query dataset. We then conducted a Pearson's correlation across all groups and visualized the integrated cell distributions using UMAP. This confirmed our q1 and q2 quiescent clusters were most similar to the S2 cluster from Shin et al., but less similar to the S1 cluster which anchors the quiescent end of the pseudotime.[40]

Single-cell RNA-sequencing analyses

RNA velocity

RNA Velocity (velocyto.R.0.6)[46] was used to forecast the future expression state of individual cells. The vector flows, representing the direction and magnitude of changes in gene expression for each cell, were utilized within a manifold constricted from the gene expression data. The velocity magnitude and directions within this manifold were then used to identify clusters serving as either the source or sink of the trajectory. Count estimates of unspliced and spliced mRNA were computed with the following parameters: velocyto run_smartseq2-d $Bamlocation $mm10_rmsk.gtf.gz –o $output, where the repeat masker files were generated from the UCSC browser. The resulting matrix of unspliced, spliced, and spanning estimates were filtered using the default setting and imported into the 'gene.relative.velocity.estimate' function using PCA embeddings to calculate cell distance. Default settings were used except for the cell kNN pooling, for which we used a k of 10 and a fit quantile of 0.2. Top genes with >0.6 gamma fit were subsetted to confirm the directionality of trajectory. This generated vectors for each cell, identifying a change in expression in the original cell state and the predicted cell state at future time t identified across the pseudotime trajectory. The rate of transcription was designated by the vector magnitude. Velocity vectors were visualized using UMAP embedding.

Cell scores

A Cell Cycle Score was calculated for each cell by taking the average of the S score and G2/M score assigned using the Seurat 'CellCycleScoring' function. A higher score indicated higher expression of S or G2/M phase markers, while a lower score indicated that cells were likely not cycling and/or in G1 phase. An Adult NSC Score was calculated for each cell using expression of quiescent adult hippocampal NSC enriched genes identified in a previous single-cell RNA-seq dataset.[34] In the previous dataset, adult hippocampal

quiescent NSCs and their immediate progeny were aligned in a pseudotime trajectory, and the top 1000 downregulated genes across the pseudotime were identified as quiescent adult hippocampal NSC enriched genes.[34] The average expression of these 1000 genes was used to calculate an Adult NSC Score for each cell.

Pseudotime trajectory

To construct the active to quiescent NSC trajectory, we loaded relevant clusters (a1, q1, and q2) of P3, P7, and P14 cells into Monocle using the default 'dpFeatures' and ICA DDRTree method along with a census method using uniform option processing for pseudotime projection. The root state was identified as a cluster with steady-state velocities and the state contained the majority of cells with the earliest developmental age for each individual analysis. A single main active to quiescent trajectory was used and divided into two separate trajectory paths (a1-q1 and q1-q2) as no major branching or deviation off the core cellular trajectory from active to quiescence was expected.

Gene regulatory network (GRN) analysis: SCENIC

To identify steady-state regulons within a particular cluster, we used the SCENIC R package (v.1.2.4)[146] algorithm, which was run on the RNA slotted Seurat matrix, which included library size normalized data. Default filtering parameters and settings were used to subset the log-transformed expression matrix and build a GRN by first using GENIE3[156] to identify potential targets for each transcriptional regulator based on inferred co-expression, which identifies non-linear relationships of genes, formatting the identified targets into co-expression modules. Then, using RcisTarget, over-represented and putative regulons were identified via DNA motifs and pruned using *cis*-regulatory motif analyses from co-expression modules mm10__refseq-r80__10kb_up_and_down_tss.mc9nr.feather. Finally, to match cell states and cell types with regulators, network activity in each cell was identified by scoring each regulon in the cell by calculating area under the curve using AUCell. We set seed for GENIE3 for reproducibility as it is based on a Random Forest approach.

CellRouter

For dynamic transcriptional regulator analysis across pseudotime, we applied the CellRouter[57] GRN analysis feature using Monocle-imported pseudotime applied to normalized data. We considered genes above the 80% quantile as positively correlated with the trajectory progression and genes below the 10% quantile as anti-correlated with the trajectory progression. These selected genes were then used to create a global GRN by sub-setting identified transcriptional regulators and using a *Z* score threshold to identify regulatory interactions via the CLR algorithm.[157,158] GRN scores ranked transcriptional regulators based on correlation with progression, the correlation of transcriptional regulator predicted targets, the number of targets and the Spearman's rank correlation.

Kinetic patterns of gene expression

To identify genes with similar expression patterns across each step of the pseudotime, we used CellRouter's[57] 'smoothDynamics', which uses loess regression to predict gene expression, and 'clusterGenesPseudotime', which uses partitioning around medoid (PAM) clustering. Gene patterns were extracted and visualized with Monocle using 'plot_pseudotime_heatmap' function.

Gene ontology (GO) analysis

To map enrichment patterns of gene ontology (GO) terms of biological processes onto the kinetic patterns of gene expression, we applied the ''compareCluster'' function from clusterProfiler (v. 3.19.1)[144,159] with default parameters to the full gene list outputted from the kinetic clustering identified by CellRouter. A full list of GO terms is summarized in Table S3. GO terms with <4 counts were removed and semantic simplification of GO terms was conducted at a 0.7 redundancy rate to identify globally significant terms. A *p*-value threshold of 0.05 was initially used to identify potentially significant results. Subsequently, the false discovery rate (FDR) was controlled at a q-value threshold of <0.2 to refine the selection of significantly enriched Gene Ontology (GO) terms.

Measuring global translation levels with OPP incorporation

OPP incorporation into *ex vivo* hippocampal slices was used to measure acute global translation levels in DG NSCs in *Hopx*^{3FlagGFP} mice at P7 and P14. *Ex vivo* acute slices were used because OPP did not cross the blood-brain barrier very well, despite reaching peripheral organs, like the liver, when OPP was injected intraperitoneally *in vivo* (data not shown). All samples (P7 and P14) were processed (dissections, OPP incorporation, staining, imaging) in parallel on the same day to reduce variability. Brains were rapidly dissected from *Hopx*$^{3FlagGFP/+}$ mice and sliced coronally into 400 μm thick slices in ice-cold, oxygenated cutting solution (206 mM Sucrose, 2.8 mM KCl, 1.25 mM NaH_2PO_4, 26 mM $NaHCO_3$ 26 mM, 1 mM $CaCl_2$ $2H_2O$, 2 mM $MgSO_4 7H_2O$, 1 mM $MgCl_2 6H_2O$, 0.4 mM Sodium Ascorbate, 10 mM D-Glucose) on a vibratome (Leica VT 1200S) at 0.30 mm/s feed speed and 1.35 mm amplitude adjustment. Brain slices were cut within 20 min of dissection and were transferred into room temperature, oxygenated aCSF (124 mM NaCl, 2.8 mM KCl, 1.25 mM NaH_2PO_4, 26 mM $NaHCO_3$, 2 mM $CaCl_2 2H_2O$, 2 mM $MgSO_4 7H_2O$, 0.4 mM Sodium Ascorbate, 10 mM D-Glucose) where they were equilibrated for 1 h. After the initial recovery period, brain slices were transferred to a new holding experimental chamber where they were incubated in 20 μM OPP in oxygenated aCSF for 1 h. Brain slices were immediately fixed in 4% PFA for 15 min and then cryoprotected in 30% sucrose solution in 1x PBS overnight at 4°C. Brain slices were frozen in TFM Tissue Freezing Medium (GeneralData) and stored at −80°C until they were re-sliced and coronal brain sections (10 μm) were collected onto Fisherbrand Superfrost Plus Microscope Slides (Fisher Scientific, 12-550-15) using a cryostat (Leica, CM3050S). Slides with re-sliced brain sections were stored at −20°C until staining was performed.

OPP was detected using the Click-iT Plus OPP Alexa Fluor 647 Protein Synthesis Assay Kit (Invitrogen, C10458) per the manufacturer's guidelines. Immunohistochemistry was performed immediately following OPP detection as described above, and all steps were performed in the dark to preserve the OPP fluorescent signal. Stained brain sections were imaged using a 40X objective on

a Zeiss LSM 810 confocal microscope (Carl Zeiss). For each 400 μm thick brain slice that was re-sliced, 3 single-plane images of the DG were collected from 3 different brain sections. The exact same imaging settings (laser power and gain) were used to image sections stained in parallel to reduce variability.

Primary cortical astrocyte culture

Primary cortical astrocyte cultures were prepared as previously described.[160] Cerebral cortices were dissected from brains of GFP-LC3 transgenic[66,160] or non-transgenic neonatal mice at P0-P1. Cortical tissue was digested using 0.25% trypsin for 10 min at 37°C, then triturated with a 5-mL pipet to break up large pieces of tissue, and then triturated with a P1000 pipet until a homogeneous suspension was achieved. Cells were passed through a 40-μm pore cell strainer (Falcon Brand Products, 352,340) and plated at a density of 2,000,000–3,000,000 cells per 10-cm dish. Cells were plated and grown in glial media (DMEM [Thermo Fisher Scientific/Gibco, 11965084] supplemented with 10% heat inactivated fetal bovine serum [Hyclone, SH30071.03], 2 mM Glutamax [Thermo Fisher Scientific/Gibco, 35,050–061], 100 U/ml penicillin and 100 μg/mL streptomycin [Thermo Fisher Scientific/Gibco, 15140122]) at 37°C in a 5% CO_2 incubator. The day after plating, and every 3–4 days following, glia were fed by replacing the glial media. After reaching 75–90% confluence (~8–10 days after plating), astrocytes were trypsinized and plated for experiments. Prior to media changes, or splitting, the culture dishes were tapped to dislodge any microglia which were then discarded with the media change. Glia were plated at a density of 225,000 cells per 35-mm fluorodish (World Precision Instruments, FD35-100) coated with 500 μg/mL poly-L-lysine (Sigma, P2636) for live-cell imaging. Astrocytes were grown in glial media for 5 DIV at 37°C in a 5% CO_2 incubator.

Primary cortical astrocyte cultures were incubated with Autophagy Assay Kit (Red) (1x concentration per manufacturer's guidelines, Abcam) for 1 h at 37°C before live imaging to detect co-localization of GFP-LC3 and Autophagy Assay Kit (Red) dye. Live cell imaging was performed on a BioVision spinning disk confocal microscope system with a Leica DMi8 inverted widefield microscope, a Yokagawa W1 spinning disk confocal, and a Photometrics Prime 95B scientific complementary metal-oxide-semiconductor camera, and an environmental chamber to maintain temperature at 37°C. Images were acquired with the VisiView software using a 63x/1.4 NA plan apochromat oil-immersion objective and solid-state 488 nm and 561 nm lasers for excitation. Z-stacks spanning the entire depth of the cell were acquired at 0.2 μm sections. Primary cortical astrocyte cultures were imaged immediately following treatment in HibE (Brain Bits, HE-Lf) imaging solution supplemented with 2% B-27, 2 mM Glutamax, 100 U/mL penicillin and 100 μg/mL streptomycin.

Flow cytometry and analysis

Dentate gyrus dissection and dissociation

DG was rapidly dissected from fresh *Hopx*$^{3FlagGFP/+}$ mouse brain in ice-cold DPBS under a dissecting microscope. Tissue was then dissociated using a MACS Neural Tissue Dissociation Kit with Papain (Miltenyi Biotec, 130-092-628) according to the manufacturer's guidelines. Dissociated cells were washed in Hank's balanced salt solution (HBSS) (PAA; GE Healthcare), the cell pellet was resuspended in 1 mL of growth medium (neurobasal medium + B27 + 1x Glutmax + 1x PenStrep) or HBSS, and the single cell suspension was filtered through a 40 μm cell sieve (Falcon; BD Biosciences).

Metabolic dye labeling

After DG dissection and dissociation, cell suspensions were incubated with Autophagy Assay Kit (Red) (1x concentration per manufacturer's guidelines, Abcam), MitoTracker Deep Red FM (25 nM, Thermo Fisher Scientific) and dihydroethidium (DHE; 5 μM, Thermo Fisher Scientific), along with the live/dead vitality dye, DAPI (1:2500 dilution, BD Biosciences), for 30 min at 37°C. Post incubation, the cells were centrifuged to remove excess dye, resuspended in PBS and immediately subjected to flow cytometry.

Autophagic flux measurement

Acute treatment with autophagy inhibitors, chloroquine or bafilomycin A1[67,68], was used to assess autophagic flux *ex vivo* because chloroquine did not reliably cross the blood-brain barrier (data not shown). After DG dissection and dissociation, cell suspensions were incubated in media (without growth factors) with either (1) saline or chloroquine (10 μM, Sigma-Aldrich), or (2) DMSO or bafilomycin A1(10 nM, Sigma-Aldrich) for 3 h at 37°C. During the last 30 min of incubation, the cells were additionally incubated with the metabolic dyes and DAPI as described above. Post incubation, the cells were centrifuged to remove excess dye, resuspended in PBS and immediately subjected to flow cytometry.

Flow cytometry and data analysis

Flow cytometry[72] was conducted on a BD FACSymphony A3 Cell Analyzer (BD Biosciences). Compensation experiments were extensively performed with single-dye staining of each dye and FMO (fluorescence minus one) controls, at all specific ages. Gating was performed to exclude dead cells and doublets (Figure S5A). The levels of the metabolic dyes within GFP^+ and GFP^- cells were both evaluated. FlowJo (V10.7.1) was used to perform all cytometric analyses.

Tamoxifen injection

A stock solution of 66.67 mg/mL tamoxifen (Sigma, T5648) was prepared in a 5:1 solution of corn oil:ethanol at 37°C with occasional vortexing until dissolved. Tamoxifen was injected intraperitoneally into *Hopx-CreER*^{T2}*::mTmG; Atg5*$^{w/w}$ and *Hopx-CreER*^{T2}*::mTmG; Atg5*$^{Flx/Flx}$ mice at 333 mg/kg on P1.

QUANTIFICATION AND STATISTICAL ANALYSIS

For quantification of cell cycle, ≥3 tiled images of the entire DG region were imaged per mouse from 4 to 12 mice at P1, P3, P7 and P14. Brain sections of equivalent dorsal-ventral location were quantified for each immunostaining set to control for any differences along the dorsal-ventral axis of the hippocampus. ≥300 GFP^+ cells from the entire DG (P1, P3, P7) or from the entire SGZ (P14) were quantified using the Point Tool in ImageJ.

For quantification of NFIX and SOX9, ≥2 images of the entire DG region were imaged per mouse from 3 mice at P7 and P14. Brain sections of equivalent dorsal-ventral locations were quantified for each immunostaining set to control for any differences along the dorsal-ventral axis of the hippocampus. The mean intensity of NFIX or SOX9 was measured in ≥300 GFP^+ cells throughout the entire DG region (P7) or throughout the entire the SGZ region (P14). A GFP^+ cell was identified, a region of interest was drawn around the nucleus of the GFP^+ cell, and the Measure function in ImageJ was used to quantify the mean intensity of staining. Then, MCM2 status was noted for each cell.

For quantification of acute global translation levels, the mean intensity of OPP was measured in ≥300 GFP^+ cells throughout the entire DG region (P7) or throughout the entire the SGZ region (P14). A GFP^+ cell was identified, a region of interest was drawn around the cell body of the GFP^+ cell, and the Measure function in ImageJ was used to quantify the mean intensity of OPP. Then, MCM2 status was noted for each cell.

For quantification of GFP^+ cells in *Hopx-CreER^{T2}::mTmG; Atg5$^{Flx/Flx}$* and *Hopx-CreER^{T2}::mTmG; Atg5$^{w/w}$* DG, samples were blinded to genotype and 3 tiled mages of the entire DG region were imaged per mouse from 4 mice per genotype at P7 and P14. GFP^+ cells from the entire DG region (P7) or from the entire SGZ and granule cell regions (P14) were quantified using the Point Tool in ImageJ. GFP^+ cells were then assessed for colocalization with other markers, such as HOPX, MCM2 or PROX1. Volumetric analyses were performed by measuring the volume of the entire DG region (P7) or the granule cell layer (P14).

Statistical analysis was performed using GraphPad Prism version 9.00 (GraphPad Software Inc.) or R. Detailed tests are listed in each figure legend.